R3-B.2: Advanced Imaging & Detection of Security Threats Using Compressive Sensing

I. PARTICIPANTS

Faculty/Staff			
Name	**Title**	**Institution**	**Email**
Jose Martinez	PI	NEU	jmartine@ece.neu.edu
Juan Heredia Juesas	Post-Doc	NEU	j.herediajuesas@neu.edu
Graduate, Undergraduate and REU Students			
Name	**Degree Pursued**	**Institution**	**Month/Year of Graduation**
Galia Ghazi	PhD	NEU	8/2017
Chang Liu	PhD	NEU	12/2019
Ali Molaei	PhD	NEU	6/2019
Richard Obermeier	PhD	NEU	12/2018
Luis Tirado	PhD	NEU	12/2018
Weite Zhang	PhD	NEU	12/2020
Anthony Bisulco	BS	NEU	6/2018
Alexis Costales	BS	NEU/REU	5/2021
Christopher Gehrke	BS	NEU	5/2021
Katherine Graham	BS	NEU	5/2021
Diego Rojas	BS	NEU/REU	5/2021
Joseph Von Holten	BS	NEU	5/2021
Diego Cachay	High School	Boston Latin School	5/2017
Nabil Kebichi	High School	Lexington High School	6/2018
Liane Xu	High School	Boston Latin School	6/2018
Alex Zhu	High School	Wayland High School	5/2017

II. PROJECT DESCRIPTION

A. Project Overview

As the problem of identifying suicide bombers wearing explosives concealed under clothing becomes increasingly important, it becomes essential to detect suspicious individuals at a distance. Systems which employ multiple sensors to determine the presence of explosives on people are being developed. Their functions include observing and following individuals with intelligent video, identifying explosives residues or heat signatures on the outer surface of their clothing, and characterizing explosives using penetrating X-rays [1, 2], terahertz waves [3-5], neutron analysis [6, 7], or nuclear quadrupole resonance (NQR) [8, 9]. At present, radar is the only modality that can both penetrate and sense beneath clothing at a distance of 2 to 50 meters without causing physical harm.

The objective of this project is the hardware development and evaluation of an inexpensive, high-resolution radar that can distinguish security threats hidden on individuals at mid-ranges (2-10 meters) using an "On-the-Move" configuration, and at standoff-ranges (10-40 meters) using a "van-based" configuration (Fig. 1).

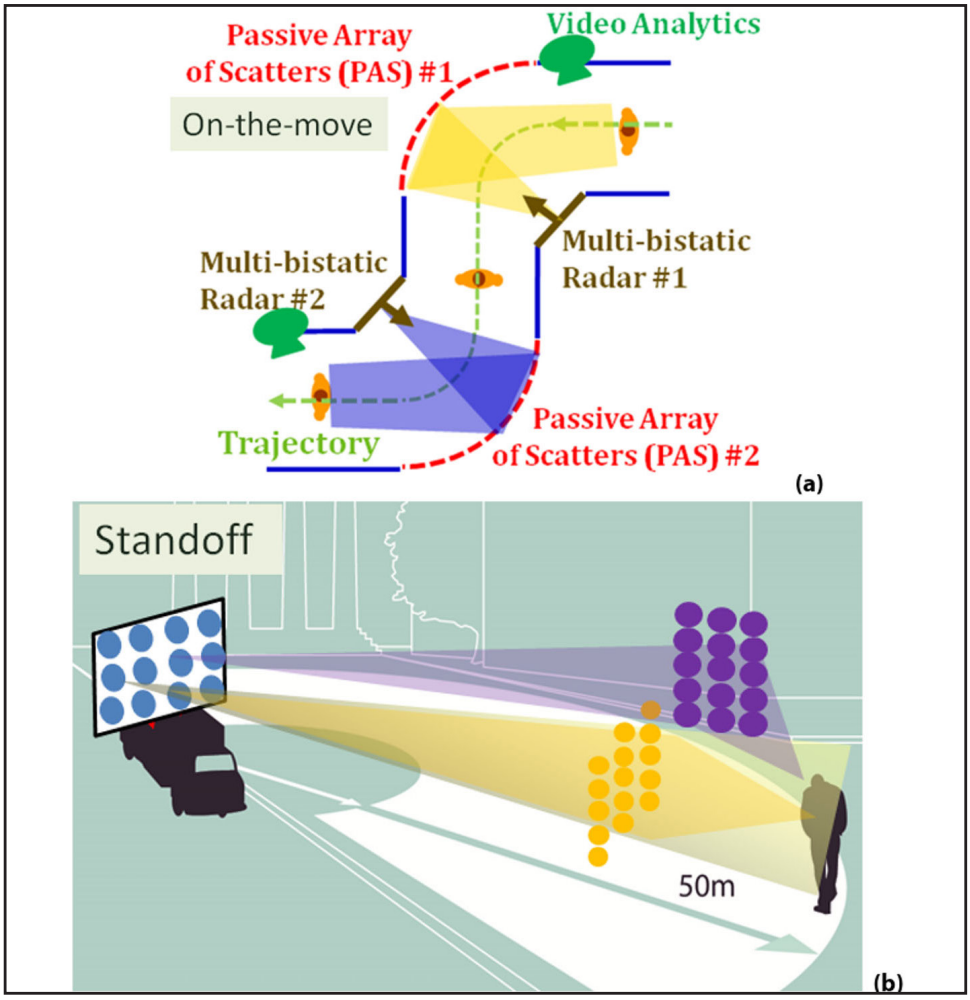

Figure 1: General sketch of the inexpensive, high-resolution radar system used for detecting security threats (a) at mid-ranges using an "on-the-move" configuration, and (b) at standoff-ranges using a "van-based" configuration.

B. State of the Art and Technical Approach

The outcome of this project would be the first inexpensive, high-resolution radar system with a special application to detect and identify potential suicide bombers. Its uniqueness is based on the ability to work on multistatic configurations, in which the information from multiple receivers and transmitters are coherently combined by using a common local oscillator. This project has the potential to be the first radar system that is capable of functioning at multiple ranges for both indoor and outdoor scenarios. An analysis of the state of the art is incorporated into Section II.C.

Table 1 shows the algorithmic development road map, including the steps needed to go from a 3D mechanical scanning imaging system (Gen-1 [10]) to a 3D fully electronic scanning imaging system (Generation 3, Gen-3 [11,12]). An intermediate imaging system (Gen-2), capable of imaging small targets in a fully electronic fashion and large targets in a hybrid electrical/mechanical fashion, will be used for a smooth transition between the Gen-1 and Gen-3 imaging systems.

Characteristics	Generation 1 – Sparse Array of Receivers	Generation 2 - Sparse Array of Transmitters and Receivers	Generation 3 - Sparse Array and Compressive Reflector Antenna
SAR imaging/ pseudo-inverse	**Task-1.1: 100% Completed** - 3D Validated with synthetic data - 3D Validated with experimental data	Non Applicable	Non Applicable
FFT imaging/ multistatic	**Task-1.2: 100% Completed** - 3D Validated with synthetic data - 3D Validated with experimental data	Non Applicable	Non Applicable
CS imaging/ Nesterov-Based	**Task-1.3: 100% Completed** - 3D Validated with synthetic data - 3D Validated with experimental data	**Task-2.3: (Y4: 60%, Y5:100%)** - 3D Validated with synthetic data - *Pending:* 3D Validated with experimental data	**Task-3.3: (Y4:50%, Y5: 75%)** - 3D Validated with synthetic data and point-like scatters - *Pending:* 3D Validated with experimental data
CS imaging/ ADMM	Non Applicable	**Task-2.4: (Y4: 60%, Y5:100%)** - 3D Validated with synthetic data and point-like scatters. - *Pending:* 3D Validated with experimental data	**Task-3.4: (Y4:50%, Y5: 75%)** - 3D Validated with synthetic data and point-like scatters - *Pending:* 3D Validated with experimental data
CS-High Capacity Sensing Design	Non Applicable	Non Applicable	**Task-3.5: (Y4:50%, Y5: 75%)** - 2D design - *Pending:* 3D design and experimental validation
New CS Imaging Algorithms	Non Applicable	**Task-2.6: (Y4: 60%, Y5:100%)** -*Pending:* 3D Validation with synthetic and experimental data	**Task-3.6: (Y4:0% , Y5: 75%)** - *Pending:* 3D Validation with synthetic and experimental data

Table 1: Algorithmic development roadmap towards a fully electronic radar imaging system; from Gen-1 [10] to Gen-3 [11, 12].

The following activities were developed for this project: 1) Alternating Direction Method of Multipliers (ADMM)-based Compressive Imaging using synthetic and experimental data of the Gen-2 system and a potential Gen-3 system configuration (Tasks 2.4 and 3.4); 2) new Compressive Imaging Algorithms using synthetic data (Task 2.6); and 3) design of a high-capacity sensing system for Compressive Sensing (CS) imaging applications (Task 3.5). This project is intimately related to ALERT Project R3-B.1, "Hardware design for 'Stand-off' and 'On-the-Move' Detection of Security Threats," because it develops the imaging algorithms for the Project R3-B.1 hardware system. As a result of the ALERT Biennial Review conducted in March of 2018, this project was terminated and will not be funded in Year 6; however, aspects of this project will be merged into Project R3-B.1. Many of the technologies and techniques developed for this project are commonly used in near-field applications by other ALERT projects, including Projects R3-A.2 and R3-A.3.

C. Major Contributions

A summary of the Year 5 major contributions can be found in Table 2.

- **C.1 - ADMM-based Compressive Imaging (Tasks 2.4 and 3.4) - This year the main outcomes of this task have been the following:**
  - **Outcome 1.1 – ADMM-based Imaging using Elastic Net regularization.**
  - **Outcome 1.2 – Consensus and Sectioning-based ADMM Compressive Imaging using rows and columns division of the sensing matrix.**
  - **Outcome 1.3 – Some results of the ADMM-based Compressive Imaging algorithms.**
    - **Outcome 1.3.1 – Validation of the ADMM with simulated data.**
    - **Outcome 1.3.2 – Validation of the ADMM with real data.**
- **C.2 – New Compressive Imaging Algorithms (Tasks 2.6) -**
  - **Outcome 2.1 – Sensing Matrix Design via Capacity Maximization for Block Compressive Sensing Applications.**
- **C.3 - Design of a high-capacity sensing system for Compressive Sensing imaging applications (Task 3.5) - This year the main outcomes of this task have been the following:**
  - **Outcome 3.1 - Compressive Imaging of extended human-size regions using an array of CRAs**

Table 2: Summary of this year's major contributions.

D. Milestones

D.1. ADMM-based Compressive Imaging (Tasks 2.4 and 3.4)

The research on the ADMM-based algorithms continued this year, exploiting the separability of the objective function and exploring new regularization functions. Specifically, the use of the Elastic Net regularization, which is a combination of the norm-1 and norm-2 regularizations, allows for a sparse solution while minimizing the risk of error. This has been proven to be very efficient when dealing with noisy data. Furthermore, exploiting the distributed capabilities of the ADMM, the analysis of the division of the sensing matrix of the system by rows and columns has been carried out, leading to the consensus and sectioning-based ADMM. Dividing the sensing matrix by rows accelerates the imaging process, and dividing the sensing matrix by columns reduces the amount of information that is required to be shared among the computational nodes. Finally, the ADMM compressive imaging has been tested with real data.

D.1.a. ADMM-based Imaging Using Joint Elastic Net Regularization

The main advantage of the ADMM resides in its property of separating the objective and the regularization terms in different variables and optimizing them in an alternative fashion. This fact allows for the use of diverse regularizations with just simple variation in the standard algorithm schemes. The Elastic Net regularization, a combination of the norm-1 and norm-2 regularizations, is a clear example of that. This regularization is expressed in the following form:

$$g_\alpha(\mathbf{v}) = (1-\alpha)\|\mathbf{v}\|_1 + \alpha\frac{1}{2}\|\mathbf{v}\|_2^2, \quad (1)$$

where the parameter α weights between the norm-1 regularization only ($\alpha = 0$) and the norm-2 regularization only ($\alpha = 1$). This enables the possibility of finding many other solutions different from the sparsest or the minimum energy solutions. Figure 2 represents graphically a 2D example of this.

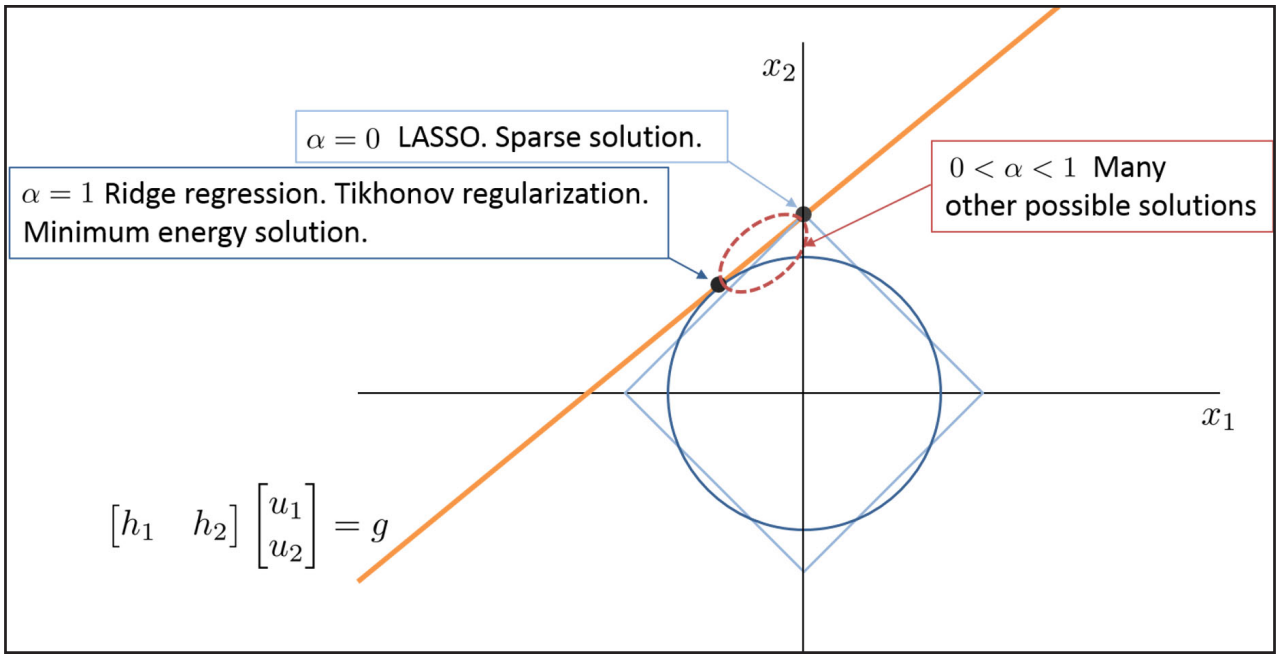

Figure 2: Optimal solutions for norm-1, norm-2, and Elastic Net regularization in a 2D example.

Given the linear problem

$$\mathbf{g} = \mathbf{H} \cdot \mathbf{u} + \mathbf{w}, \tag{2}$$

where $\mathbf{g} \in \mathbb{C}^{N_m}$ is the vector of measurements, $\mathbf{H} \in \mathbb{C}^{N_m \times N_p}$ is the sensing matrix, $\mathbf{w} \in \mathbb{C}^{N_m}$ represents the noise collected by the receiver, and $\mathbf{u} \in \mathbb{C}^{N_p}$ is the unknown complex vector; the Elastic Net regularization consensus ADMM problem is defined as follows:

$$\begin{aligned} \text{minimize } & \frac{1}{2}\sum_{i=1}^{M} \|\mathbf{H}_i\mathbf{u}_i - \mathbf{g}_i\|_2^2 + \lambda\left((1-\alpha)\|\mathbf{v}\|_1 + \alpha\frac{1}{2}\|\mathbf{v}\|_2^2\right) \\ \text{s.t. } & \mathbf{u}_i - \mathbf{v} = 0 \quad \forall i = 1, \ldots, M \end{aligned} \tag{3}$$

where $\mathbf{H}_i$ are row block submatrices of the sensing matrix $\mathbf{H}$, and $\mathbf{g}_i$ are subvectors of $\mathbf{g}$. The variables $\mathbf{u}_i$ are copies of the unknown vector $\mathbf{u}$, which are used for solving the problem for each $\mathbf{H}_i$ and $\mathbf{g}_i$. The constraint forces that all partial solutions agree through the variable $\mathbf{v}$.

This problem is solved by the following iterative scheme:

$$\mathbf{u}_i^{k+1} = (\mathbf{H}_i^*\mathbf{H}_i + \rho\mathbf{I})^{-1}\left(\mathbf{H}_i^*\mathbf{g}_i + \rho(\mathbf{v}^k - \mathbf{s}_i^k)\right) \tag{4.a}$$

$$\mathbf{v}^{k+1} = \frac{1}{1+\frac{\alpha\lambda}{\rho M}} S_{(1-\alpha)\lambda/\rho M}\left(\bar{\mathbf{u}}^{k+1} + \bar{\mathbf{s}}^k\right) \tag{4.b}$$

$$\mathbf{s}_i^{k+1} = \mathbf{s}_i^k + \left(\mathbf{u}_i^{k+1} - \mathbf{v}^{k+1}\right) \tag{4.c}$$

where ρ is the augmented parameters, $S_t(a)$ is the soft-thresholding operator, and $\mathbf{s}_i^{k+1}$ is the dual variable at iteration k+1. Notice that these equations are very similar to the simple norm-1 regularized consensus-based ADMM. The only difference appears in the solution of the consensus variable $\mathbf{v}$. Now this variable combines the shrinkage properties of both norm-1 and norm-2 regularization, depending on the value of α. On one

hand, the soft-thresholding operator forces small input values to be zero, due to the norm-1 regularization. On the other hand, the non-zero output values are decreased due to the norm-2 regularization. Figure 3 represents graphically this double shrinkage.

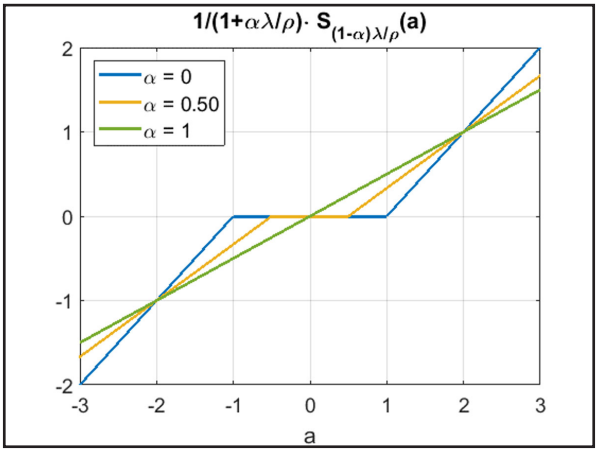

Figure 3: Graphical representation of the weighted soft-thresholding operator in terms of the parameter *α*.

D.1.b. Consensus and Sectioning-based ADMM Using Rows and Columns Division of the Sensing Matrix

The consensus-based ADMM has been proven to accelerate the convergence and perform imaging in quasi real-time by diving the sensing matrix by rows and optimizing different replicas of the unknown vector in parallel with less data for each one [12, 13], but it has the drawback of slow communication among the computational nodes, since the whole imaging vector needs to be transmitted at each iteration. This problem has been addressed by dividing the sensing matrix in columns instead of rows. In this way, the amount of information to be transmitted among the nodes is drastically reduced. This idea led to sectioning the imaging domain in several sub-regions and optimizing them independently, sharing small pieces of information at each iteration. Combining both techniques, a parallel and distributed algorithm with a reduced communications among the computational nodes is achieved.

Considering the same problem as in Equation (2), let us divide the sensing matrix into *M* row block and *N* column block sub-matrices, as shown in Figure 4.

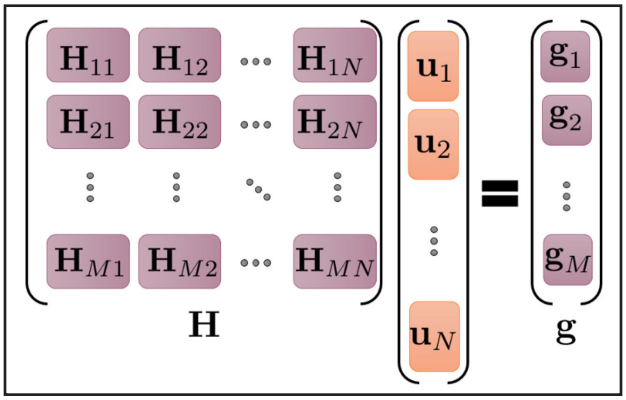

Figure 4: Representation of the division of the matrix sensing system by rows and by columns.

The problem to solve is now of the following form:

$$\begin{aligned} &\text{minimize } \frac{1}{2}\sum_{\mathrm{i}=1}^{M}\left\|\sum\nolimits_{\mathrm{j}=1}^{N}\left(\mathbf{H}_{\mathrm{ij}}\mathbf{u}_{\mathrm{j}}^{\mathrm{i}}-\mathbf{g}_{\mathrm{i}}\right)\right\|_{2}^{2}+\lambda\sum\nolimits_{j=1}^{N}\left\|\mathbf{v}_{\mathrm{j}}\right\|_{1} \\ &\text{s.t.}\quad \mathbf{u}_{\mathrm{j}}^{\mathrm{i}}-\mathbf{v}_{\mathbf{j}}=0\quad \forall \mathrm{i}=1,\ldots,M,\qquad \forall \mathrm{j}=1,\ldots,N \end{aligned} \tag{5}$$

where is the i-th replic of the j-th sub-vector of the unknown vector . The solution of this optimization problem is given by the following iterative scheme:

$$\mathbf{u}_{j}^{i,(\mathrm{k}+1)}=\left(\mathbf{H}_{ij}^{*}\mathbf{H}_{ij}+\rho\mathbf{I}_{\frac{N_p}{N}}\right)^{-1}\left(\mathbf{H}_{ij}^{*}\mathbf{g}_{ij}^{(\mathrm{k})}+\rho\left(\mathbf{v}_{j}^{(k)}-\mathbf{s}_{j}^{i,(\mathrm{k})}\right)\right) \tag{6.a}$$

$$\mathbf{v}_{j}^{(k+1)}=S_{\lambda/M\rho}\left(\bar{\mathbf{u}}_{j}^{(k+1)}+\bar{\mathbf{s}}_{j}^{(k)}\right) \tag{6.b}$$

$$\mathbf{s}_{j}^{i,(\mathrm{k}+1)}=\mathbf{s}_{j}^{i,(\mathrm{k})}+\left(\mathbf{u}_{j}^{i,(\mathrm{k}+1)}-\mathbf{v}_{\boldsymbol{j}}^{(\mathrm{k}+1)}\right) \tag{6.c}$$

where

$$\mathbf{g}_{ij}^{(\mathrm{k}+1)}=\mathbf{g}_{\boldsymbol{i}}-\sum_{\substack{q=1\\ q\neq j}}^{N}\mathbf{H}_{iq}\mathbf{u}_{q}^{i,(\mathrm{k})}=\mathbf{g}_{\boldsymbol{i}}-\sum_{\substack{q=1\\ q\neq j}}^{N}\hat{\mathbf{g}}_{iq}^{(\mathrm{k})} \tag{6.d}$$

and $\bar{\mathbf{u}}_{j}^{(k+1)}$ and $\bar{\boldsymbol{s}}_{j}^{(k+1)}$ are the mean of $\mathbf{u}_{j}^{i,(k+1)}$ and $\mathbf{s}_{j}^{i,(k+1)}$, respectively, for all replicas *i* of a given segment *j*, at iteration k+1.

This problem splits the imaging domain in several regions (division by columns) and then, for each one, some replicas are created (division by rows) and optimized independently, as shown in Figure 5. Figure 6 shows the architecture of the computational nodes distribution and their connections.

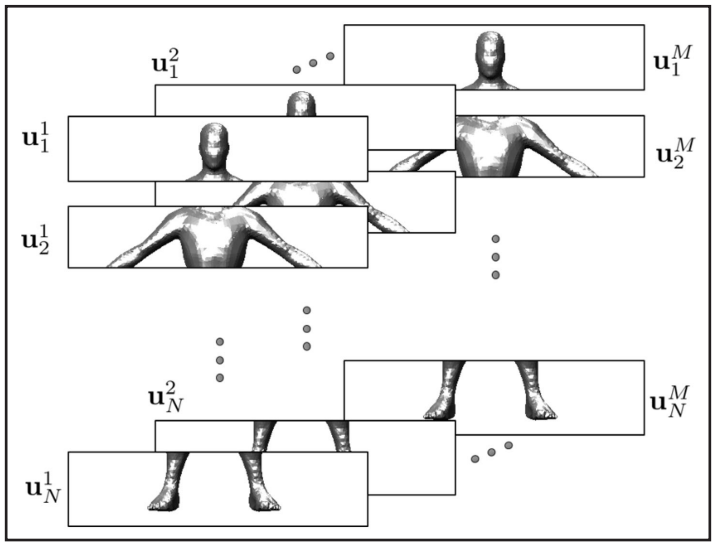

Figure 5: Graphical interpretation of the division by rows and columns. The image is sectioned into N regions, and each of them are replicated M times for performing the imaging with few data allocated to each node. The solution for each region is an average-like of all the replicas. The final imaging solution is the concatenation of all the regions.

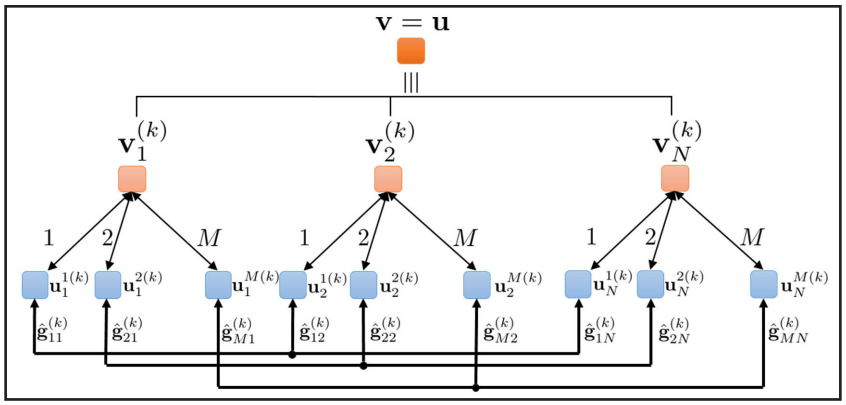

Figure 6: Architecture of the consensus and sectioning-based ADMM. The problem is split into N nodes, each of them acting as a central node that collects the updates of M sub-nodes, computes the soft-thresholding operator of the mean of them, and then distributes the solution again to the sub-nodes. Each sub-node shares, for each iteration, a small vector dependent on their local optimization with the remaining sub-nodes that correspond with the same replica.

In terms of the communications among the computational nodes, Figure 7 shows a comparison among the consensus-based (division by rows), the sectioning-based (division by columns), and the consensus and sectioning-based ADMM algorithms, meanwhile Table 3 shows the amount of elements that need to be interchanged by one node at each iteration.

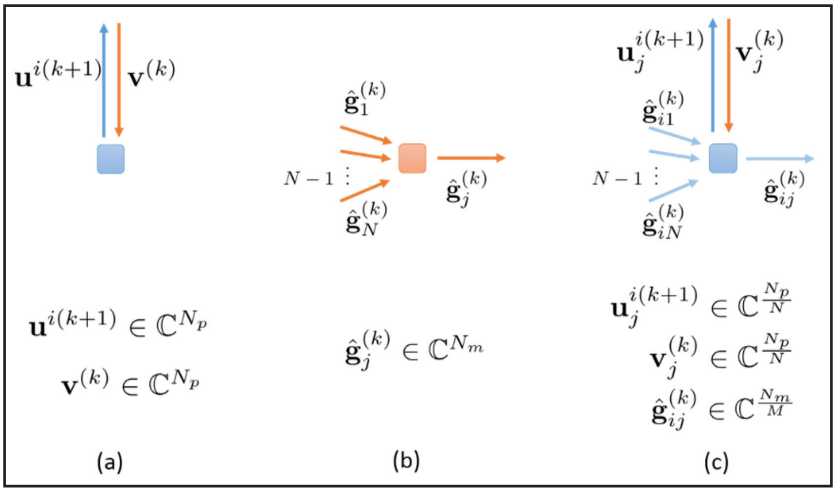

Figure 7: Schematic representation of the vectors and their lengths that are received from and transmitted by one single node at iteration *k* when the sensing matrix of the problem is divided in submatrices (a) by rows, (b) by columns, and (c) by both rows and columns.

ADMM method	**# of elements shared for one node at iteration k**
Consensus-based (Rows-wise division)	$2N_p$
Sectioning-based (Columns-wise division)	$N \cdot N_m$
Consensus and Sectioning-based (Rows and columns-wise division)	$N\frac{N_m}{M} + 2\frac{N_p}{N}$

Table 3: Number of elements to be shared for one single node at one iteration for the three ADMM distributed techniques.

Therefore, depending on the known ratio $R = {}^{N_p}\!/_{N_m}$ between the number of pixels in the imaging domain and the number of measurements, selecting one or other techniques will be more efficient in terms of communications among the computational nodes. The graphics plotted in Figure 8 compare these techniques for different values of the parameter R.

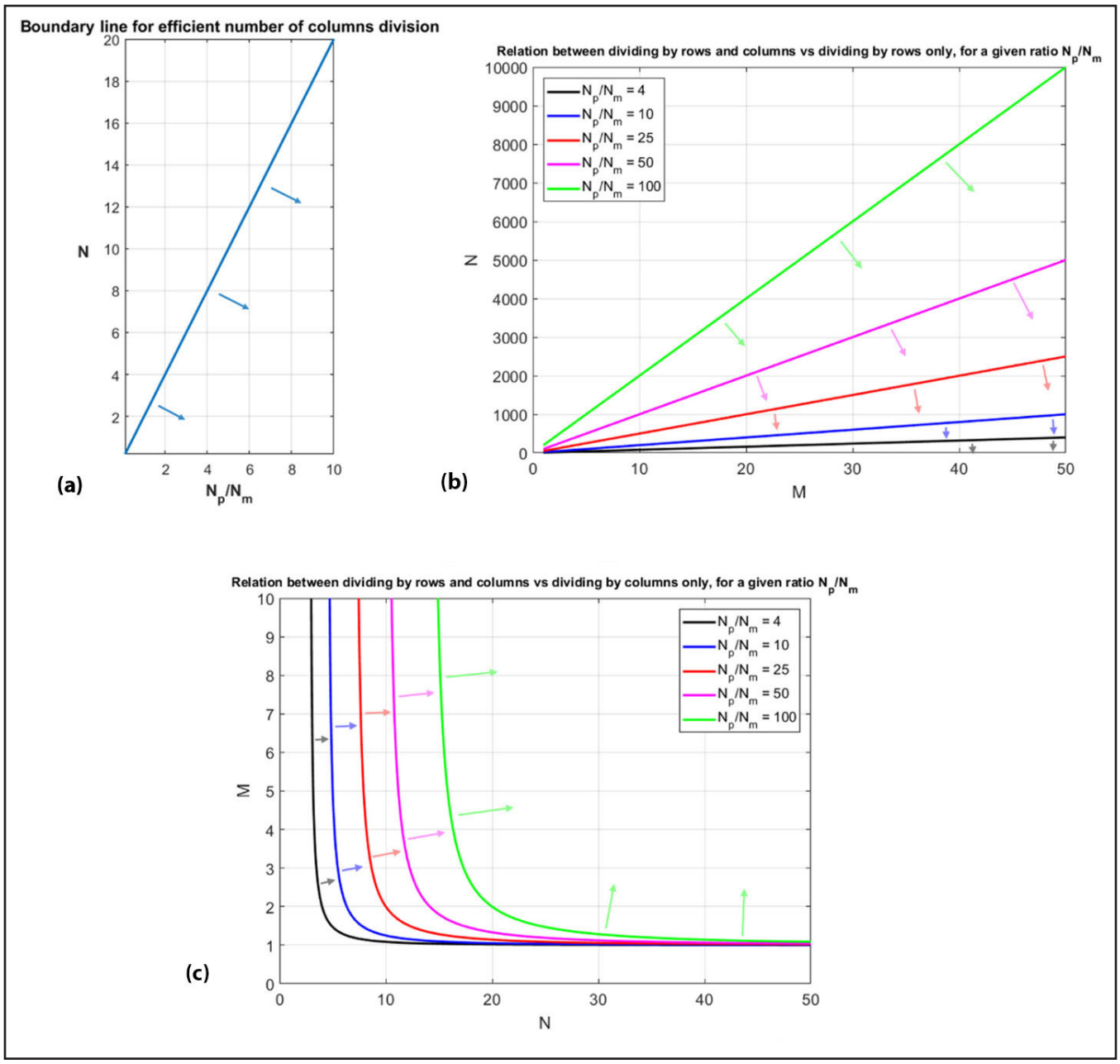

Figure 8: (a) Column-wise division vs. row-wise division. Dividing the sensing matrix in submatrices by columns is more efficient, in terms of communications among nodes, than dividing it by rows for the integer and positives values of N that fall in the area indicated by the arrows, given R. (b) Row and column-wise division vs. row-wise division. Dividing the sensing matrix in submatrices by rows and columns is more efficient, in terms of communications among nodes, than dividing it by rows only for the integer and positive values of M and N that fall in the area indicated by the arrows, for a given ratio R. (c) Row and column-wise division vs. column-wise division. Dividing the sensing matrix in submatrices by rows and columns is more efficient, in terms of communications among nodes, than dividing it by columns only for the integer values of N and M that fall in the area indicated by the arrows, for a given ratio R.

D.1.c. Some Results of the ADMM-based Compressive Imaging Algorithms.

D.1.c.i. Simulated Data

The Elastic-Net regularized ADMM has been tested in a problem of source reconstruction [14]. Five point sources of unit value are located in a square normalized over the wavelength λ_0 and N_{Rx} receivers are placed in a circular position of radius 10, with and angular separation of $\theta = \frac{2\pi}{N_{Rx}}$, as shown in Figure 9. The measured field is described by the following equation:

$$g_m = \sum_{n=1}^{N_p} u_n e^{-jkd_{nm}} \longrightarrow \mathbf{g} = \mathbf{Hu} \tag{7}$$

where $k = \frac{2\pi}{\lambda_0}$ and d_{nm} is the distance between the $n-th$ pixel and the $m-th$ receiver. Figure 10 shows the reconstruction error for different number of receivers for a sparsity level of $S = 5$ when varying the parameter α (from norm-1 to norm-2 regularization), for a $SNR = 50dB$. It can be seen that the minimum error is obtained for an intermediate value of α, as is also shown in Figure 11.

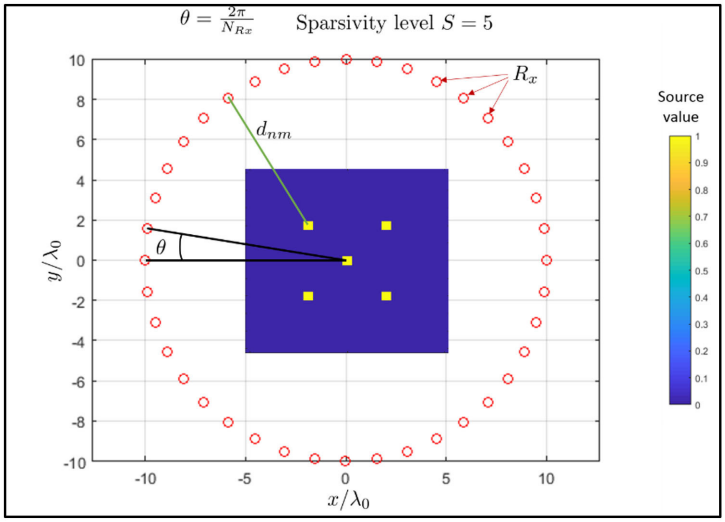

Figure 9: System configuration. Yellow points represent the sources over the dark blue square region of interest. Red circles represent the receivers. All distances are normalized by the wavelength λ_0.

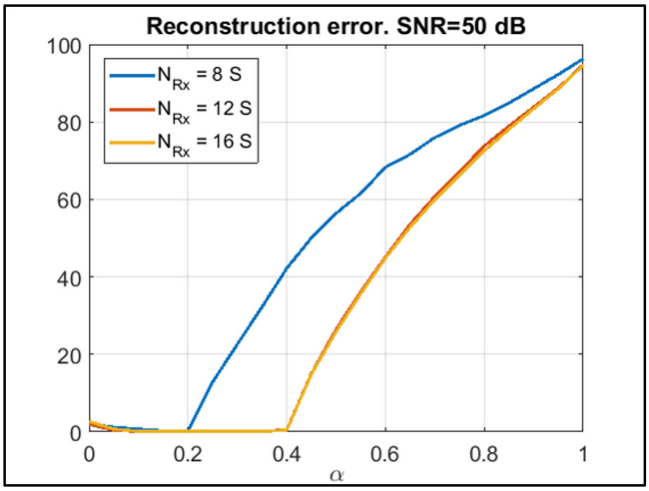

Figure 10: Reconstruction error varying the parameter α for different number of receivers with a SNR=50dB.

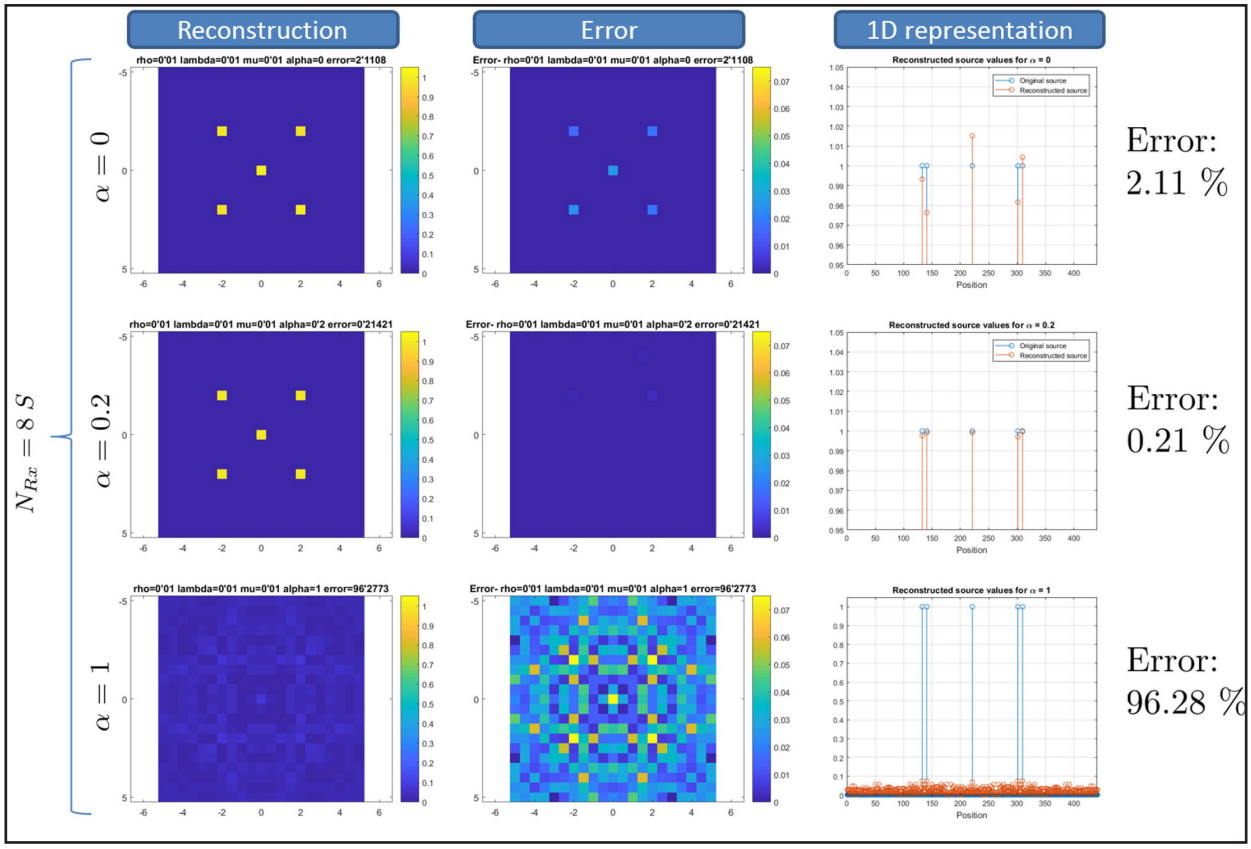

Figure 11: Source reconstruction and error when applying the Elastic Net regularized ADMM for different values of the parameter *α*.

The consensus and sectioning-based ADMM was tested via a mm-wave imaging application, through the use of two compressive reflector antennas, according to the structure described in Figure 12. Having 12 transmitters and 12 receivers and employing 15 frequencies in the 70-77GHz band, the total number of measurements is N_m = 2160 for imaging a 3D structure containing N_p = 22500 pixels. The results, when dividing the sensing matrix in M= 4 row blocks and N = 3 column blocks, are presented in Figure 13. Table 4 shows the amount of information to be shared by one single node at each iteration, being clear how the sectioning (division by columns) and consensus and sectioning-based (division by rows and columns) ADMM highly reduces this amount compared to the consensus-based ADMM (division by rows). The consensus and sectioning-based ADMM produces a good quality imaging with a reduced amount of information required to be shared among the computational nodes.

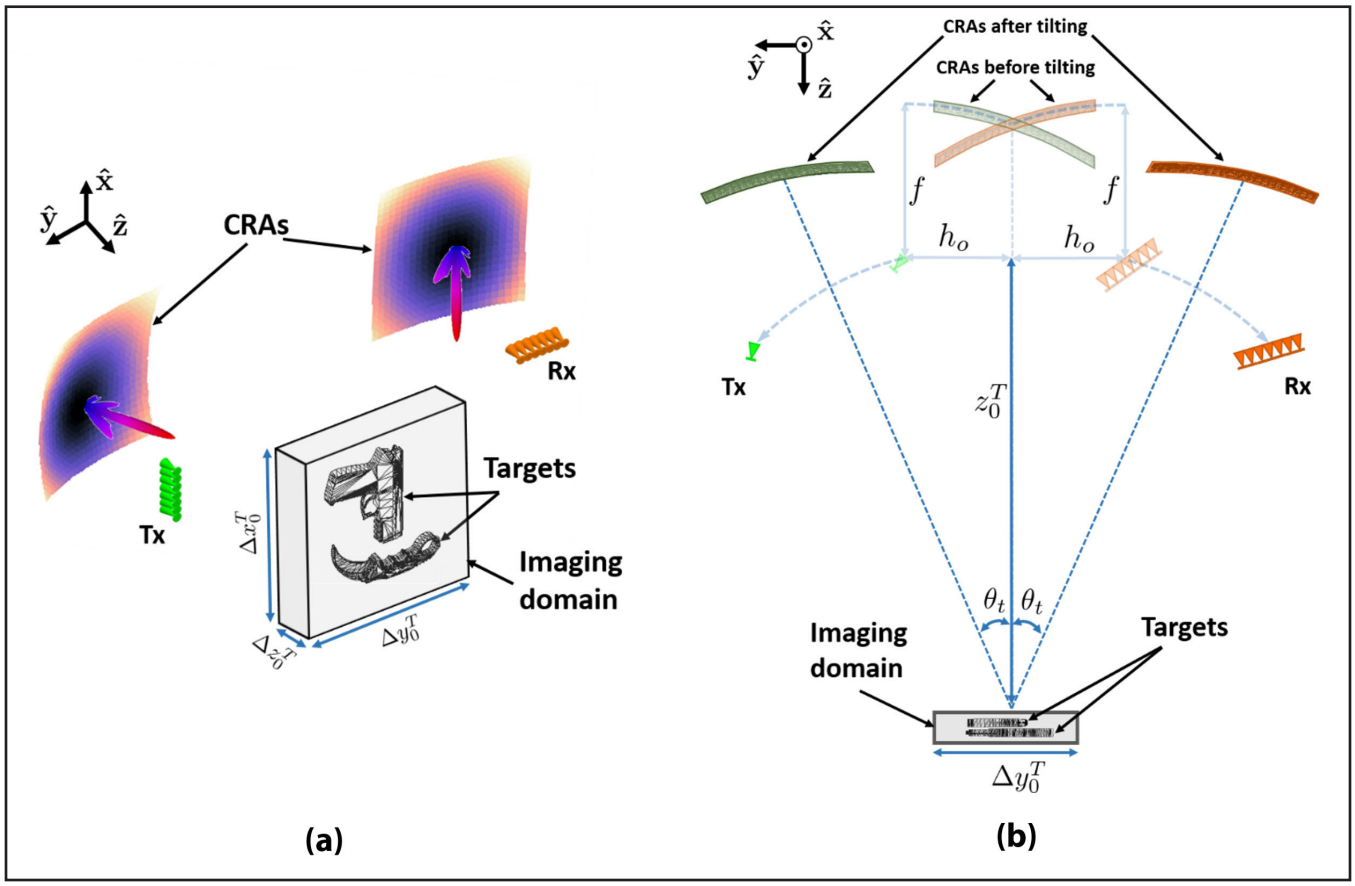

Figure 12: (a) Geometry of the sensing system. A vertical array of transmitters feed one CRA that illuminates the imaging domain. The field scattered by the targets is reflected by another CRA and measured by a horizontal array of receivers. (b) Top view of the sensing system. The faded CRAs and arrays of Tx and Rx indicate their position before tilting. The green CRA is tilted θ_t degrees in the +ŷ direction, and the orange CRA is tilted θ_t degrees in the -ŷ direction.

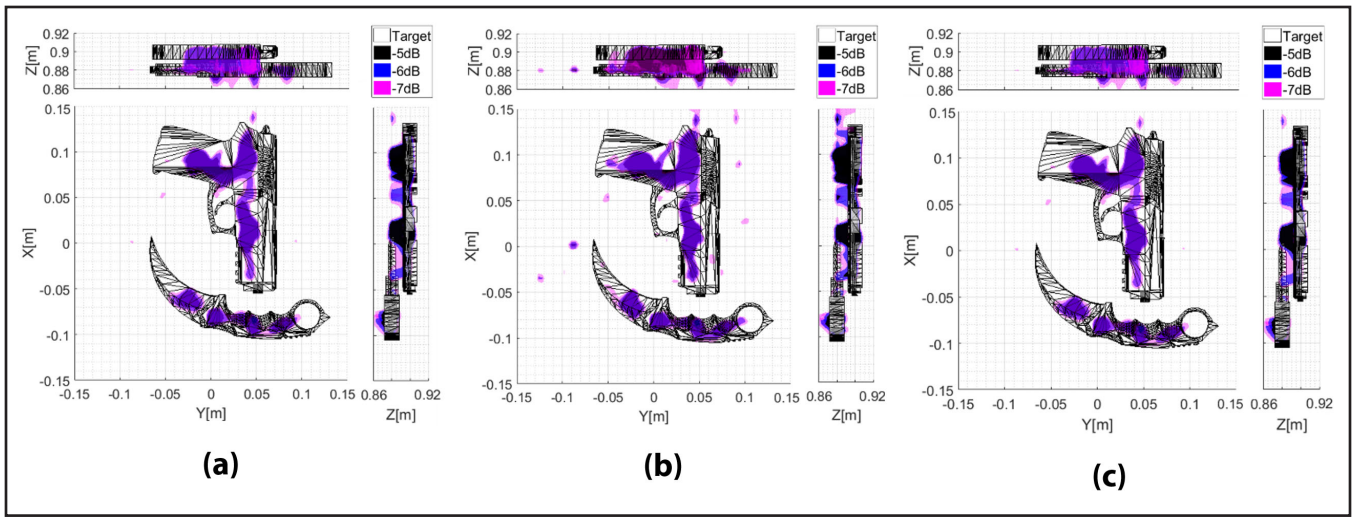

Figure 13: Imaging reconstruction (top, front, and side views) using (a) Consensus-based ADMM, (b) Sectioning-based ADMM, (c) Consensus and Sectioning-based ADMM. The targets are represented with transparent black triangles and the reconstructed reflectivity is presented in the colored map.

ADMM method	#of elements to be shared	% of element reduction with respect to the consensus-based ADMM
Consensus-based	45,000	0%
Sectioning-based	6,480	85.6%
Consensus and Sectioning based	12,870	71.4%

Table 4: Amount of information to be shared by one single node at each iteration.

D.1.c.ii. Real Data

The ADMM algorithm has been tested in real data collected in the actual configuration of the radar in our laboratory. A person with a metallic box concealed under its clothes is being imaged by the radar. After the measurements are collected, the ADMM algorithm is applied for each time frame, identifying the range of the metallic box and some parts of the human body. The imaging is performed by adding in magnitude the imaging of 10 consecutive frames. Figure 14 shows the imaging performed at one instant for different ranges, perfectly identifying the position of the metallic box. When these results are fused with the information taken from optical cameras like the Kinect, which can identify the range of the objects they are observing, the mm-wave imaging results can be refined, This is done by performing the imaging starting from the point at which the Kinect has identified the person that is walking. In this way, some energy is saved since only a small area is imaged; the imaging time is reduced, since less data is required; and we can get rid of possible artifacts that may appear in front of the person. The imaging with the ADMM can be done in just 0.3 seconds for each time frame. Placing the imaging results for each time frame, a 3D video can be created representing the mm-wave reflectivity and the depth of the target imaged. Figure 15 plots one frame of these videos.

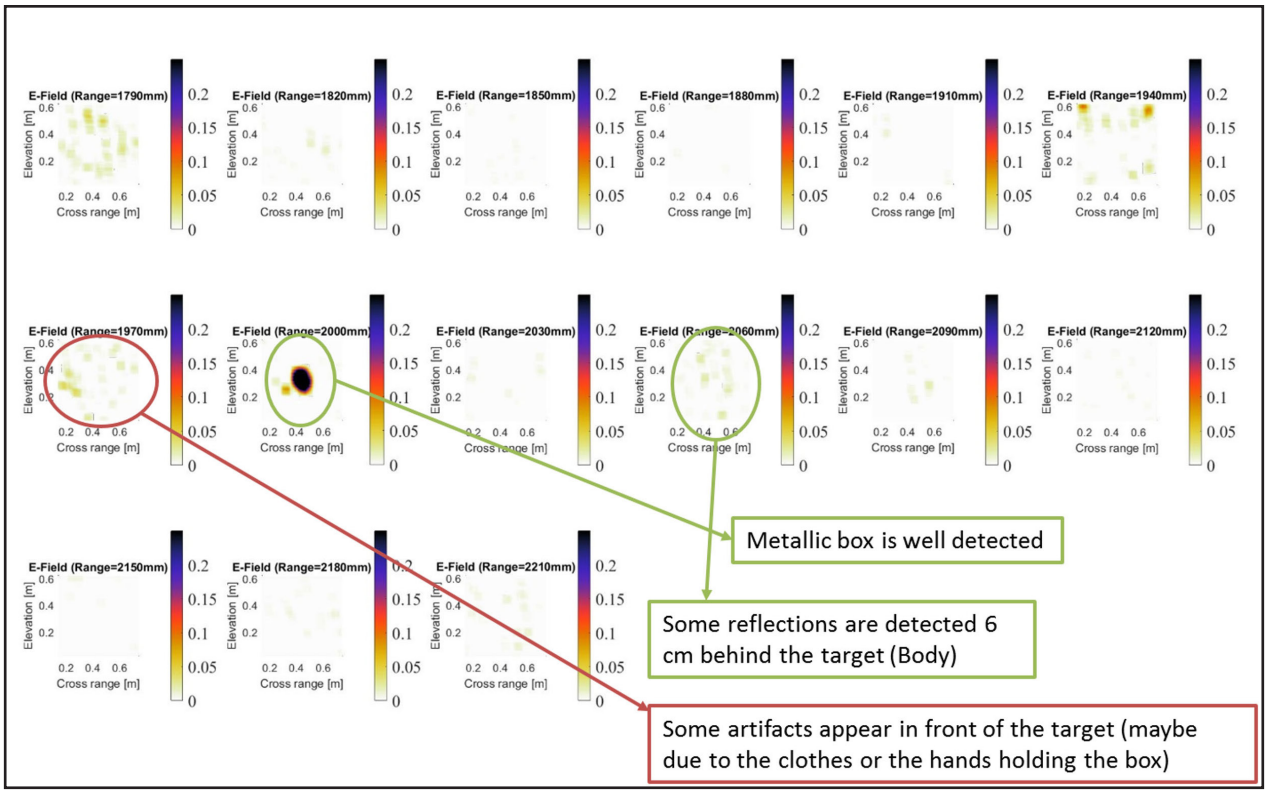

Figure 14: Imaging per range for one time frame with ADMM. The metallic box is perfectly defined and some parts of the human body behind the target. Other artifacts appear in front of the target, probably due to some reflection of the clothes and/or the hands that hold the metallic box for the experiment.

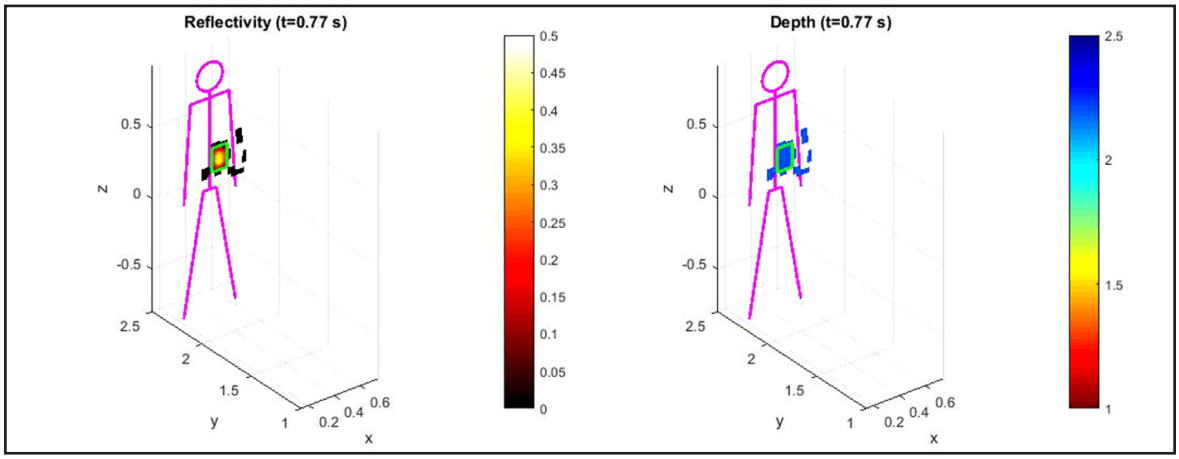

Figure 15: One time frame of the 4D (3 spatial dimension plus time) reconstructed imaging once the front layers have been removed after applying the a priori information provided by the Kinect with normalized reflectivity (left) and range position (right).

D.2. New Compressive Imaging Algorithms (Task 2.6).

In last year's report, we described how the success of Compressive Sensing (CS) techniques largely depend upon the properties of the sensing matrix A, and how the most commonly used performance metric, the Restricted Isometry Property (RIP), is not suitable for many real-world applications, such as electromagnetic imaging. To overcome this challenge, we developed a novel sensing matrix design method based upon mutual coherence minimization [15] and presented some numerical results that demonstrate the method's capabilities. Since then, we have developed an enhanced method that can be applied to block CS applications [16-17].

D.2.a. Sensing Matrix Design via Capacity Maximization for Block Compressive Sensing Applications

Block CS generalizes standard CS for applications in which the unknown signal of interest is known to exhibit block, or group sparsity. The concept of block sparsity can be simply described by Figure 16, which displays two different signals with sparsity S = 4. The block sparsity of these signals can be evaluated by first grouping the individual elements into blocks and then counting how many blocks have non-zero elements. For example, if we group samples zero and one together, then two and three, etc., for a total of four groups, the signal on the left has a group sparsity of three and the signal on the right has a group sparsity of two. Specialized reconstruction techniques that exploit group sparsity (such as joint ℓ_2/ℓ_1 minimization) have been shown to provide better reconstruction performance than standard CS techniques (such as ℓ_1 minimization). Unsurprisingly, the success of specialized block CS reconstruction techniques can be assessed using extensions to the RIP.

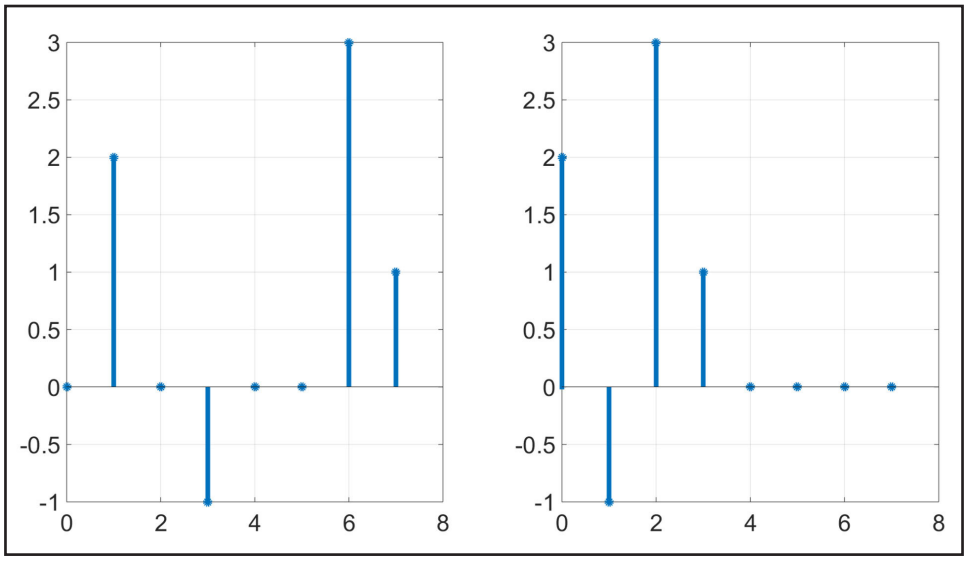

Figure 16: Two signals with sparsity S = 4, but different block sparsity based upon the grouping.

Our sensing matrix design method considers the problem of sensing matrix design from the perspective of information theory, and is formally expressed as follows. Suppose that the sensing matrix $A \in \mathbb{C}^{M\times N}$ is assumed to be a function of design variables $p \in \mathbb{C}^L$ according to the possibly nonlinear, but differentiable relationship $A = F(p)$. The design algorithm then seeks the minimizer of the following optimization program:

$$\underset{p}{\text{minimize}} \max_{r=1,\ldots,R} -\log\det(\Phi_r^T F^H(p) F(p) \Phi_r + \beta I) \tag{8}$$

$$\text{subject to } p \in Q_p$$

where Φ_r are sub-sampling matrices that extract the elements for the R different groups and Q_p defines the feasible set of values that can take. This is a nonlinear, non-convex problem, which can be solved using the Augmented Lagrangian method. In laymen's terms, the optimization problem maximizes the smallest capacity of sub-matrices obtained by selecting columns from the full sensing matrix. For a sensing matrix that is used to reconstruct a S_B block-sparse signal, where each block has L values, the algorithm can theoretically be configured to optimize over all $\binom{N/L}{2S_B}$ sub-matrices of size $M \times 2L$ to establish reconstruction guarantees using the block RIP. Unfortunately, this is not feasible in practice even for moderately sized problems. In many problems though, the algorithm can be applied over all $\binom{N/L}{2}$ sub-matrices of size $M \times 2L$ to enhance reconstruction accuracy.

To assess the capabilities of the capacity maximization design method, let us reconsider the design application described in last year's report. Consider an imaging system in which a single transmitting and receiving antenna is used to excite a region of interest with a single frequency. This antenna was constrained to operate at positions within a $5\lambda \times 5\lambda$ grid located a distance of 5λ away from the imaging region. The unknown signal of interest was known to lie within nine blocks, denoted by the shaded regions in Figure 17, which was discretized into 144 points (nine four by four blocks). The objective of the design problem was to select the locations that the antenna would operate at. Figure 17 displays the locations that the antenna operated at for the baseline design (blue) and the optimized design (red). Over the $\binom{144/16}{2} = 36$ possible combinations of blocks, the original randomized sensing matrix has a minimum capacity of -12.6, while the optimized sensing matrix has a minimum capacity of -3.6. This led to a direct improvement in reconstruction accuracy, as can be seen in Figure 18, which displays the reconstruction accuracies of the baseline random design (blue) and optimized design (red) when joint ℓ_2/ℓ_1 (block CS) and standard ℓ_1 techniques are applied.

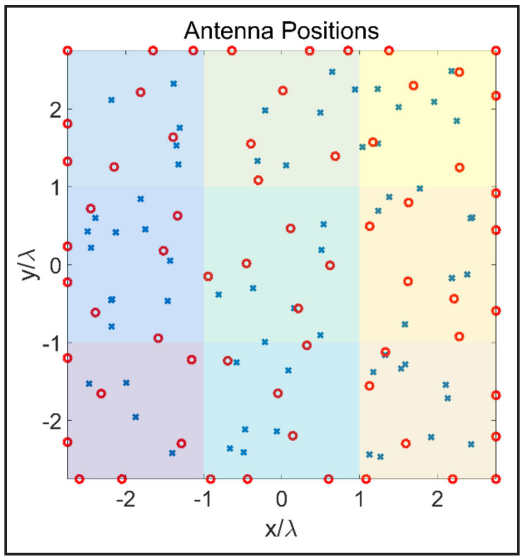

Figure 17: Antenna positions of the baseline (blue) and optimized (red) designs. The shaded boxes in the background represent the squares on which the capacity was evaluated.

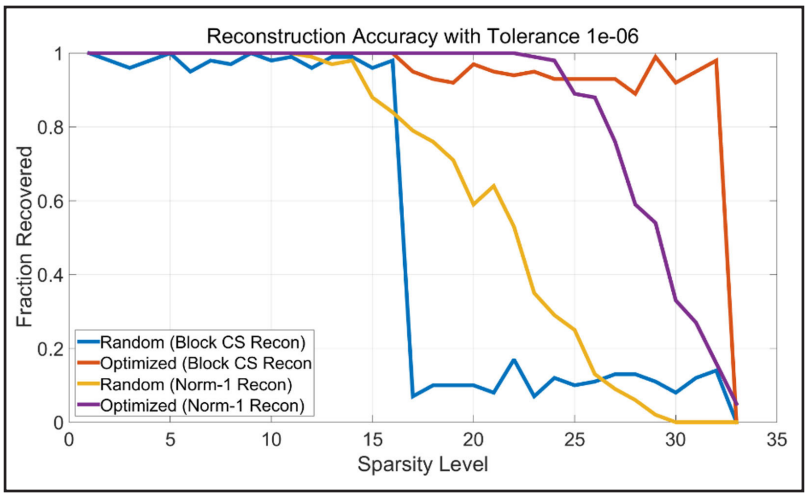

Figure 18: Numerical comparisons of the reconstruction accuracies of joint ℓ_2/ℓ_1 (block CS) and standard ℓ_1 techniques using the baseline random and optimized designs.

D.3. Design of High-capacity Sensing System for CS Imaging Applications (Task 3.5)

D.3.a. Compressive Imaging of Extended Human-size Regions Using an Array of CRAs.

As an example of the high-capacity sensing systems, an MMA-based CRA array made of eight compressive reflectors is designed, in order to be able to have a walk-through system for imaging an extended human-size region. As depicted in Figure 19, the CRA is manufactured by introducing a set of discrete applique scatterers on the surface of a traditional reflector antenna (TRA). Each CRA is illuminated with an array of transmitting and receiving antennas located on the focal plane. The electromagnetic cross-coupling between adjacent CRAs is used in order to enhance the sensing capacity of the system, as well as to extend the region that it can image. The proposed millimeter-wave sensing and imaging system is composed of eight CRAs positioned at sides of the walk through system, as shown in Figure 20a. The 3D human model was projected into a 2D plane located 2 m away from the focal plane. The coding mechanism of the CRAs relies on two principles: (1) spatial coding of the electromagnetic field, generated by introducing discrete PEC scatterers on the surface of a TRA and (2) spectral coding of electromagnetic fields, generated by 8-bit MMAs, tailored on the surface of the reflector.

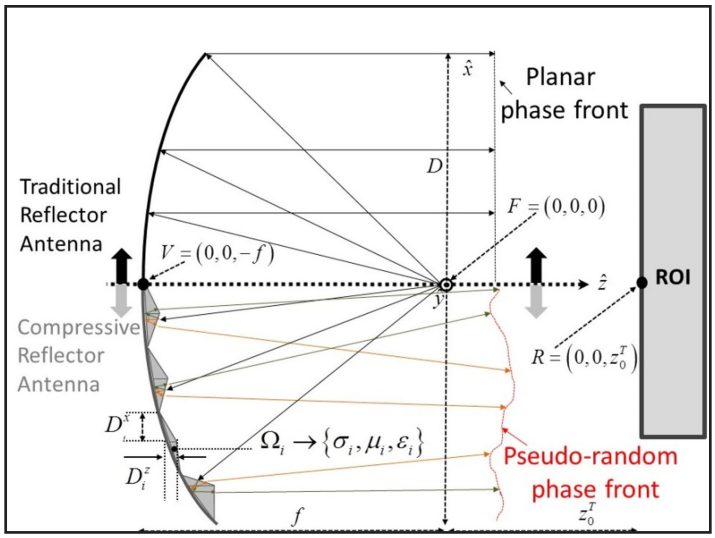

Figure 19: 2D cross-section of a Traditional Reflector Antenna (x > 0) and Compressive Reflector Antenna (x < 0).

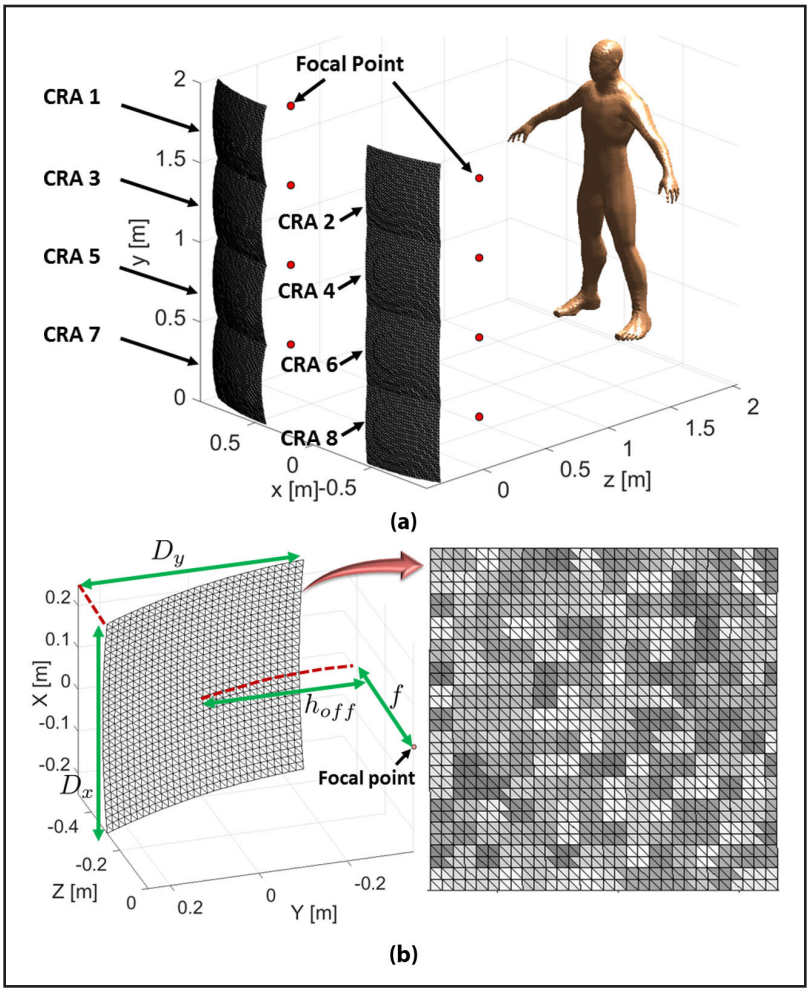

Figure 20: (a) CRA array for imaging a human model; (b) a single CRA in offset mode (left) with the 8-bit MMAs tailored on the surface of the CRA (right).

Each CRA is illuminated with two orthogonal receiving (Fig. 21a) and transmitting (Fig. 21b) arrays located on the focal plane of the reflector. The electromagnetic cross-coupling between adjacent CRAs was used to perform the imaging. Given the location of the target with respect to the array, only the electromagnetic cross-coupling between CRA-*l* and CRA-*k*: (*l*=1,*k*=2), (*l*=3,*k*=4), (*l*=5,*k*=6), (*l*=7,*k*=8), (*l*=1,*k*=4), (*l*=3,*k*=6) and (*l*=5,*k*=8) is considered.

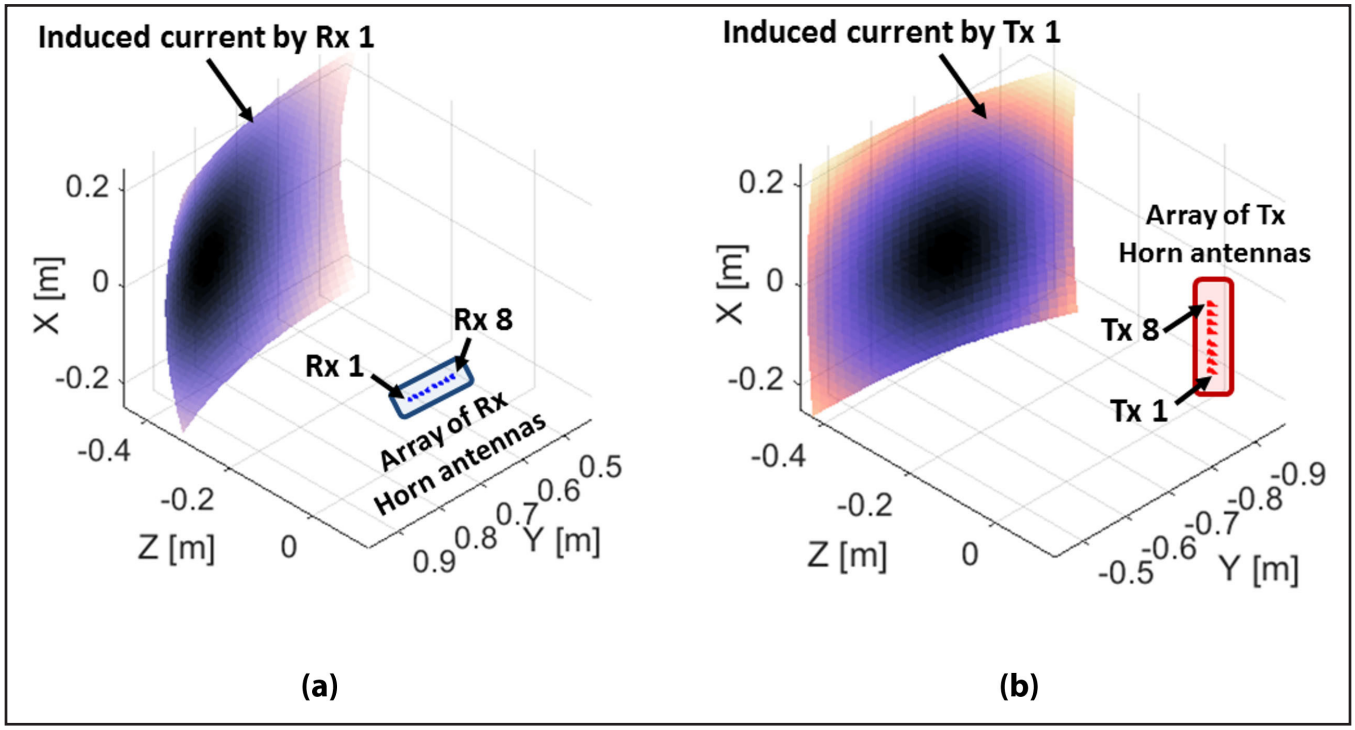

Figure 21: (a) Array of receiving horn antennas feeding the CRA-2; and (b) array of transmitting horn antennas feeding the CRA-1.

The design parameters for each one of the reflectors are shown in Table 5. Both the vertical receiving array (Fig. 21a) and the horizontal transmitting array (Fig. 21b) of each CRA consist of eight uniformly distributed conical horn antennas. With a similar procedure explained in Section E.3.a ("Design of a Compressive Reflector for Enhancing the Sensing Capacity") of last year's report, an 8-bit binary code $c_i = a_1 \ldots a_8$ ($i \in \{1, \ldots,256\}$) is associated to each MMA design. Each digit of the binary code $a_j \in \{0,1\}$ ($j \in \{1, 2, \ldots,8\}$) is associated with a resonance frequency f_j. The eight resonant frequencies are uniformly selected within the 67.375 GHz to 79.625 GHz frequency band. The reflector's surface is divided into $2^8 = 256$ sub-surfaces and is randomly coated with the 256 different MMA configurations. In Figure 20b, each gray-scale color (*rgb(i/2,i/2,i/2)*) on the surface of the reflector represents a unique MMA configuration operating with the code c_i. In Figure 22, the reflection coefficient and absorption value for eight different binary codes are plotted. Based on the resonance frequencies of the 8-bit MMAs, 66.5-80.5 GHz is selected to be the operational band of the radar and $N_f = 87$ regularly sampled frequencies are used to perform the imaging.

PARAMETER	VALUE
Frequency band	$66.5 - 80.5\ GHz$
No. of frequencies (N_f)	87
No. of $Tx.$	8
No. of $Rx.$	8
Aperture size ($D_x = D_y$)	$50\ cm$
Focal length (f)	$50\ cm$
Offset height (h_{off})	$35\ cm$
Size of the random facets	4λ
Max. Distortion of facets	$3°$

Table 5: Design parameters for a single CRA.

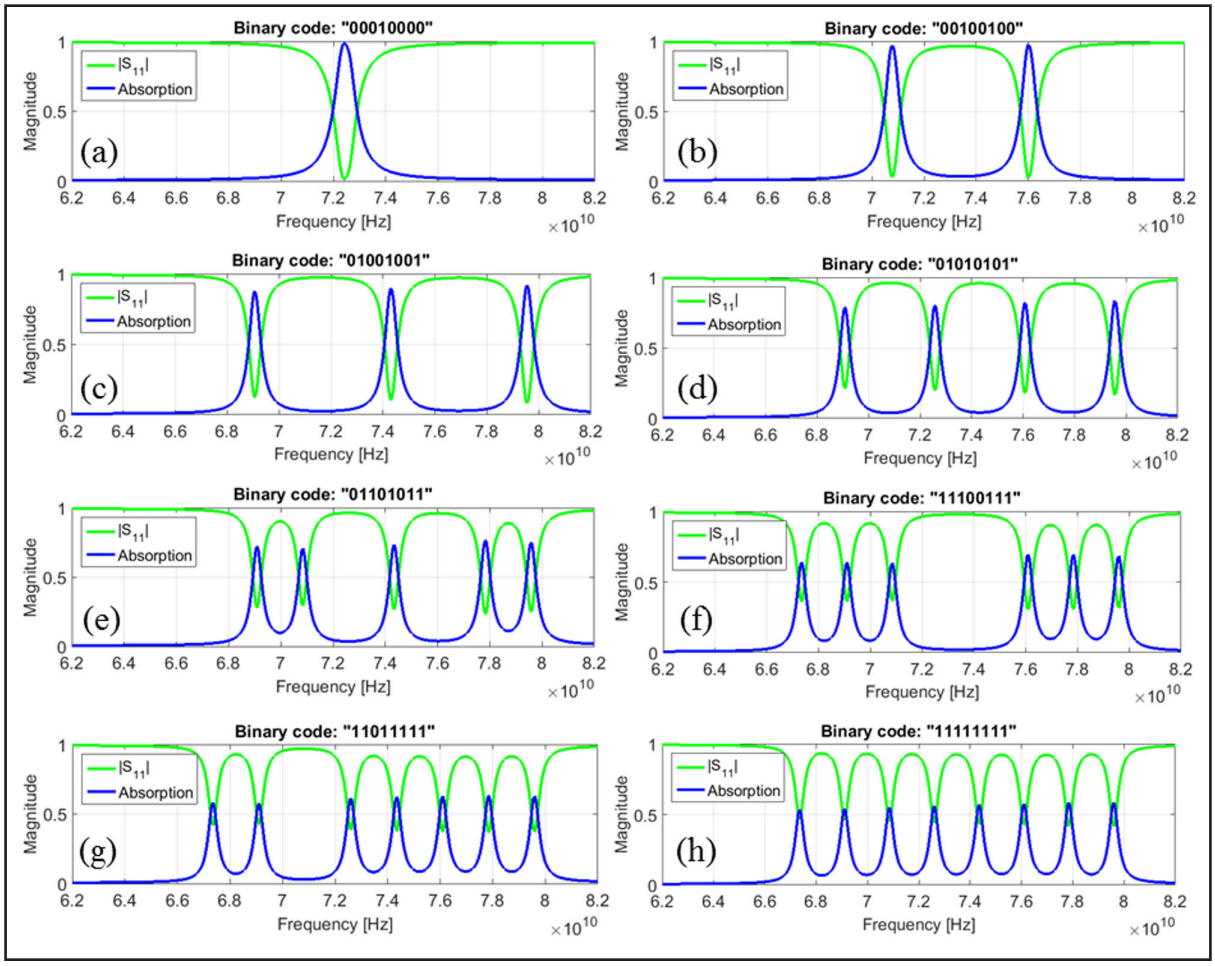

Figure 22: Magnitude of reflection ($|S_{11}|$) and absorption ($1-|S_{11}|^2$) of the MMA array for different binary codes: (a) c_{16} = 00010000, (b) c_{32} = 00100100, (c) c_{73} = 01001001, (d) c_{85} = 01010101, (e) c_{107} = 01101011, (f) c_{231} = 11100111, (g) c_{223} = 11011111, and (h) c_{255} = 11111111.

In this numerical example, the 8-bit MMAs are established in the frequency range of 66.5 GHz to 80.5 GHz, equivalent to a bandwidth of 19%, which is more than twice the bandwidth of the 4-bit MMA example presented in Section E.3.a of last year's report. Nevertheless, there have been several efforts on extending the

local periodicity approach [18], which aim at expanding application scope of the method to the cases where the variations between the elements are not smooth. As it can be seen from the results in [18], in such cases the deviations and inaccuracies predominantly occur at the side lobes while the predictions of local periodicity for the main lobe remains accurate. In the case of this example, there is not much concern about the side lobes and they do not play a major role in the near-field sensing, which makes effective medium approach valid, even if the variations between the adjacent elements are not very smooth.

Figure 23a shows the improved SV distribution of the single MMA-based CRA, when compared to that of the CRA without MMAs and a TRA. Also, Figure 23b shows how the sensing capacity of the CRA is enhanced for different SNR levels. The image reconstruction is performed using the MATLAB toolbox NESTA [19] imposing norm-1 regularization priors. The imaging result of the CRA with and without the 8-bit MMAs are plotted in Figure 24.

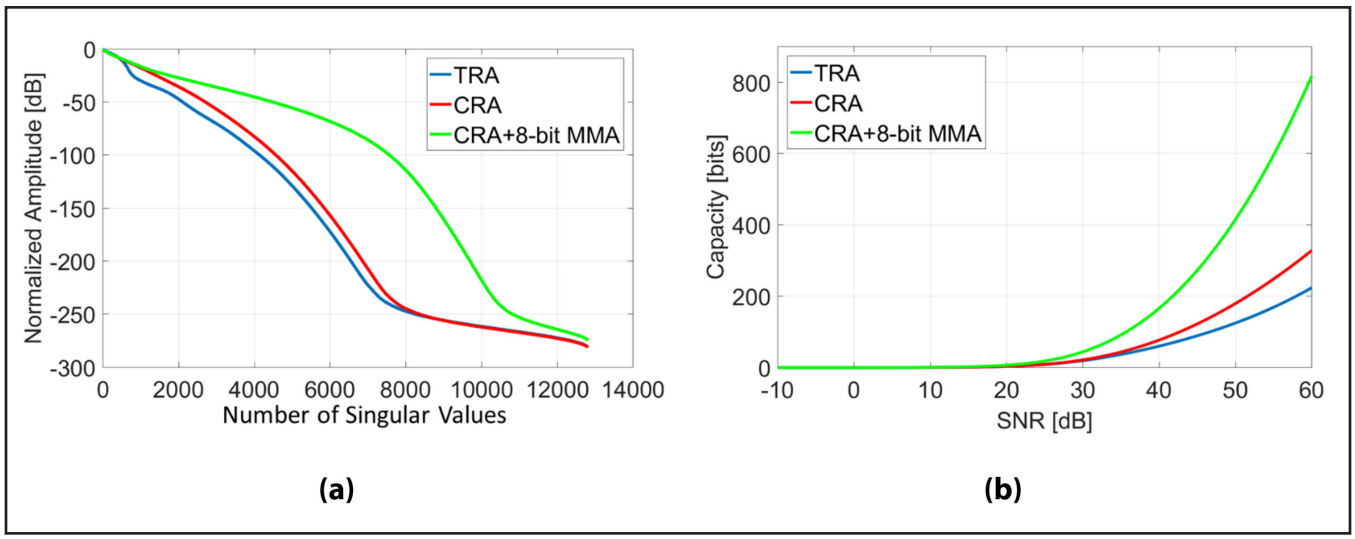

Figure 23: Comparison of (a) the normalized SV distribution and (b) the sensing capacity of a single CRA and TRA.

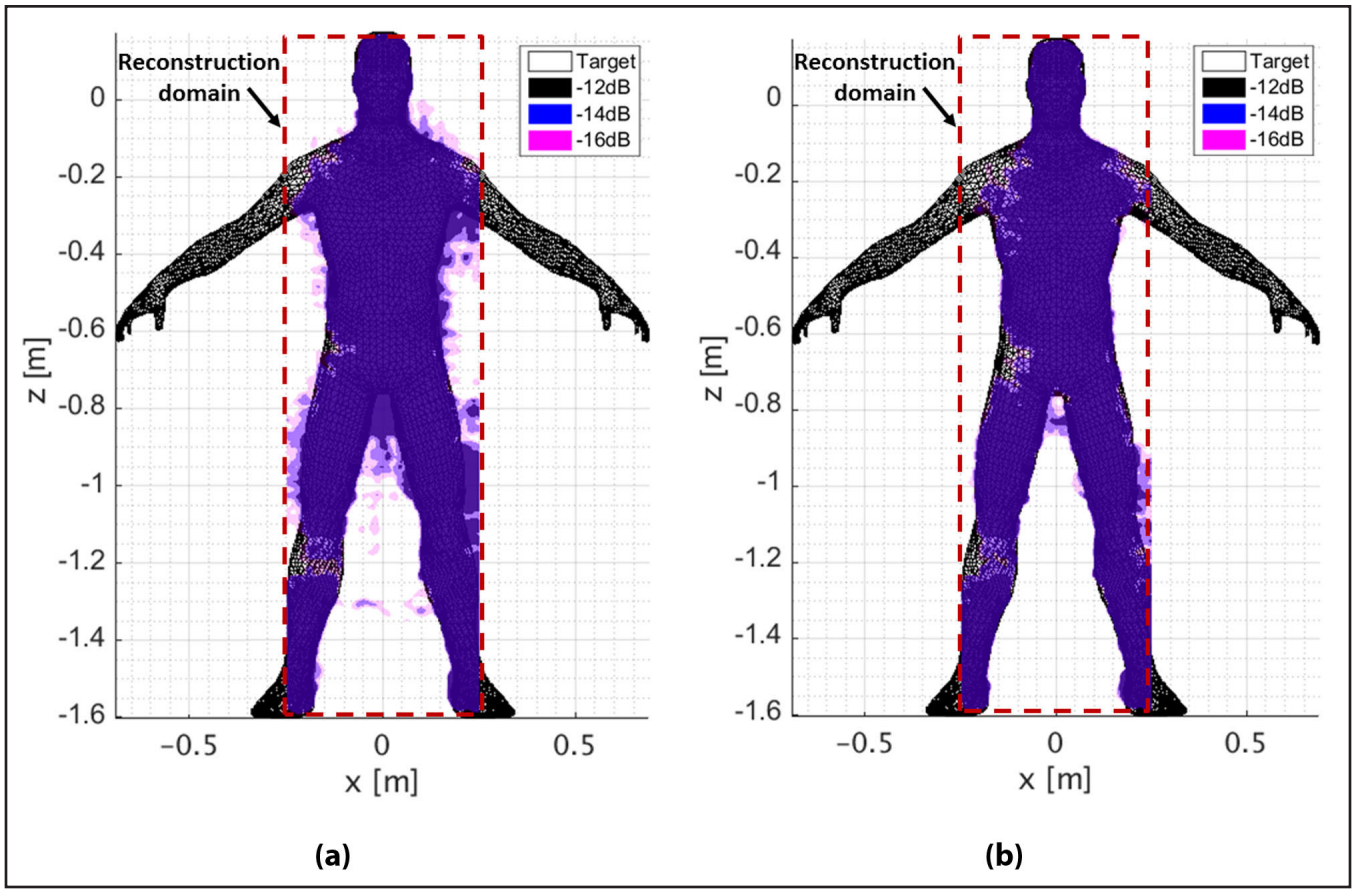

Figure 24: Reconstructed image using iterative compressive sensing algorithm (NESTA) for the (a) CRA and (b) MMA-based CRA arrays.

To justify the improvement of the MMA-based CRA compared to that of the CRA without the MMAs, the imaging accuracy for both configurations are quantitatively measured and then compared to each other. Figure 25a shows the original target mask that needs to be reconstructed. In Figures 25b and 25c, the reconstructed images above a threshold level of -16 dB are represented for the CRA and MMA-based CRA configurations, respectively. In Figures 25d and 25e, the wrong reconstructed areas (red color) and correct reconstructed areas (light blue color) are represented for the CRA and MMA-based CRA configurations. The accuracy of the imaging is calculated as the number of correct reconstruction pixels divided by the total number of pixels in the imaging domain. The wrong reconstructions could be either a point in the target domain that is detected with a reflectivity level smaller than -16 dB or a point outside the target domain that has been detected with a reflectivity level higher than -16 dB. The accuracy for the CRA configuration and MMA-based CRA configurations are calculated to be 88.74% and 92.46%, respectively, which shows the effectiveness of the established MMAs in the imaging system.

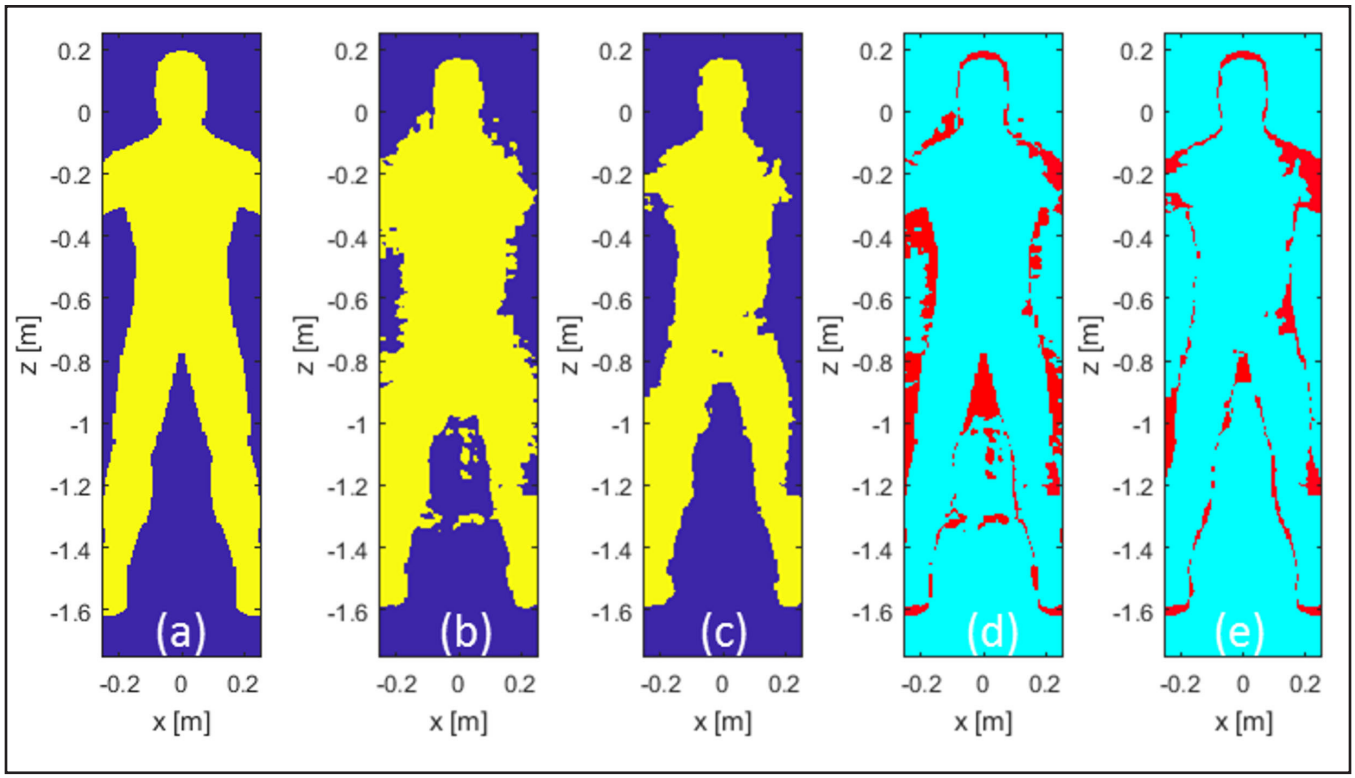

Figure 25: (a) Original target. Reconstructed image above the -16 dB threshold for the (b) CRA, and (c) MMA-based CRA configurations. Image reconstruction error (red color) for the (d) CRA, and (e) MMA-based CRA configurations.

Finally, this improvement will be even more evident for a target that is less sparse than that used in Figure 24 under a Total Variation Norm metric. Specifically, as shown in Figure 23, for a SNR=50 dB, the MMA-based CRA has about 30% more singular values above the noise level than the simple CRA; so considering a typical value on the minimum number of measurements "*m*" needed to reconstruct an "*s*"-sparse signal to be *m=4s*, then the MMA-based CRA should be able to reconstruct signals of sparsity $s_{CRA/MMA}$ = 1000, while the CRA will only be able to reconstruct signals with sparsity s_{CRA} = 750.

E. Future Plans

As a result of the ALERT Biennial Review conducted in March of 2018, this project was terminated and will not be funded in Year 6; however, aspects of this project will be merged into Project R3-B.1. Our future plans for these aspects are outlined below and in the report for Project R3-B.1.

- ADMM-based Compressive Imaging. For the next few years, the follow-on tasks and expected outcomes are the following:
  - Task 3.4 (Year 6 and beyond) – Test and validate the algorithm in the Gen-3 system using multiple CRAs. The expected outcomes are a) validation of the algorithm in 3D with synthetic and experimental data of multiple CRAs.
- Design of a high-capacity sensing system for CS imaging applications. For the next few years, the follow-on task and expected outcome are the following:
  - Task 3.5 (Years 6, and beyond) – Extend the design of the high-capacity sensing compressive reflector to 3D. The expected outcome is the design and experimental validation of a 3D Gen-3 system presenting maximum sensing capacity.

- Accelerating Compressive Imaging using multistatic FFT (including non-uniform FFT). For the next few years, the follow-on tasks and expected outcomes are the following:
    - Task 3.6 (Year 6 and beyond) – Test and validate the algorithm in the Gen-3 system. The expected outcome is the validation of the algorithm in 3D with experimental data.
- Automatic target detection using Deep Learning. For the next few years, the follow-on tasks and expected outcomes are the following:
    - Task 3.7 (Year 6 and beyond) – Create a database of different examples of targets and perform their reflectivity reconstruction via mm-wave imaging with the Gen-3 system that could serve for training and optimizing a Convolutional Neural Network (CNN) for automatic target detection. The expected outcomes are a) several mm-wave reconstruction images of a variety of metallic and no metallic targets with different shapes and locations; and b) a dataset of labels corresponding to these images, which can be used for training and optimizing a CNN, in order to perform automatic target detection.

III. RELEVANCE AND TRANSITION

A. Relevance of Research to the DHS Enterprise

The following features will be of special relevance to the Department of Homeland Security (DHS) enterprise:

- Non-invasive, minimally-disruptive "On-the-Move" scanning with quality imaging and high throughput; fast data collection in less than 10ms.
- Full body imaging with interrupted forward movement during mm-wave pedestrian surveillance; in multi-view.
- A small number of non-uniform sparse array of Tx/Rx radar modules will minimize the cost of on-the-move; five transmitters +five receivers + 10 switches.

B. Potential for Transition

The features of "On-the-Move" have attracted the attention of several industrial and government organizations.

- Industrial transition partners: HXI, Inc., L3 Communication, Rapiscan, and Smiths Detection.
- Target government customers: Transportation Security Administration (TSA), the U.S. Department of Justice (DOJ), Customs and Border Protection (CBP), and the Department of State.

C. Data and/or IP Acquisition Strategy

The hardware and algorithmic design, integration, and validation performed under this project will continue to generate IP. In the past, several provisional patents have been submitted to Northeastern University's (NEU) IP office, and our connection with different transition partners will facilitate its transition into industry. Moreover, the hardware will also be used to create benchmark datasets that may be used by industry stakeholders in order to assess the performance of their reconstruction/imaging algorithms. Moreover, a patent was awarded in Year 4 (February 21, 2017) based on the work partially done in this project: U.S. Patent 9,575,045, "Signal Processing Methods and Systems for Explosives Detection and Identification Using Electromagnetic Radiation."

D. Transition Pathway

HXI Inc. has been collaborating with our Project R3-B.1 research team. Together, HXI and ALERT have

designed, fabricated, integrated, and validated the radar system. We expect that after the assembling the first Gen-3 prototype, HXI will license our IP and transition the technology to the mm-wave imaging market. Additionally, new low-cost miniaturized modules are being developed by HXI for the next generation mm-wave system; some of these components will be tested by the Project R3-B.1 PI.

The PI has also established a working relationship with Smiths Detection and L3 Communications, which bodes well for future collaboration and transition.

E. Customer Connections

Customer Names & Program Offices:

- HXI – Mr. Earle Stewart
- Smith's Detection Systems – Dr. Kris Roe
- L3 Communications– Dr. Simon Pongratz

Frequency of Contact & Level of Involvement in Project:

- The PI has weekly meetings with HXI for the project.
- The companies Smiths Detection and L3 Communications had 3 to 4 meetings with the PI last year.

New proposals related to the topic of this research will be submitted to other federal funding agencies.

IV. PROJECT ACCOMPLISHMENTS AND DOCUMENTATION

A. Education and Workforce Development Activities

1. Course, Seminar, and/or Workshop Development
    a. Prof. Martinez-Lorenzo was invited to give a talk entitled "High Capacity and Efficiency Optimization of Compressive Antennas for Imaging Applications" at the Special Session "Inverse Problems: Theory, Techniques, and Applications," of the European Conference on Antennas and Propagation. London, UK (April 2018). This talk covered several results generated by Projects R3-B.1 and R3-B.2.
2. Student Internship, Job, and/or Research Opportunities
    a. Graduate students, Chang Liu, Ali Molaei, Luis Tirado, and Weite Zhang play an important role in our research project. They will continue to assist in the development of new hardware design and integration for the mm-wave radar system.
    b. Our undergraduate students, Anthony Bisulco, Christopher Gehrke, Katherine Graham, and Joseph Von Holten, will continue to work on Projects R3-B.1 and R3-B.2.
3. Interactions and Outreach to K-12, Community College, and/or Minority Serving Institution Students or Faculty
    a. The PI participated in the Building Bridges Program, which provides opportunities for high school students to visit NU's laboratories and gain hands-on research experience in order to engage them in STEM education.
    b. The PI participated in the Young Scholars Program at Northeastern University, in which two high school students spent 6 weeks in Prof. Martinez's lab learning about sensing and imaging.
4. Other Outcomes that Relate to Educational Improvement or Workforce Development
    a. Populating the research group with undergraduates brings homeland security technologies to

undergraduate engineering students, and establishes a pipeline to train and provide a rich pool of talented new graduate student researchers.

B. Peer Reviewed Journal Articles

1. Molaei, A., Heredia Juesas, J., Blackwell, W.J., & Martinez-Lorenzo, J.A. "Interferometric Sounding Using a Metamaterial-Based Compressive Reflector Antenna." *IEEE Transactions on Antennas and Propagation, 66*(5) pp. 2188-2198, 2018. DOI: 10.1109/TAP.2018.2809488
2. Molaei, A., Heredia-Juesas, J., Ghazi, G., Vlahakis, J., & Martinez-Lorenzo, J.A. "Digitized Metamaterial Absorber-based Compressive Reflector Antenna for High Sensing Capacity Imaging." arXiv:1806.06934.
3. Tirado, L., Ghazi, G., Alvarez-Lopez, Y., Las-Heras, F., Martinez-Lorenzo, J.A. "A GPU Implementation of the Inverse Fast Multipole Method for Multi-Bistatic Imaging Applications." *Progress in Electromagnetics Research M*, Vol. 58, 159-169, 2017. DOI: 10.2528/PIERM17021004

Pending-

1. Molaei, A., Bisulco, A., Tirado, L., Zhu, A., Cachay, D., Ghanbarzadeh Dagheyan, A., & Martinez-Lorenzo, J.A. "3D Printed E-Band Compressive Horn Antenna for High-sensing-capacity Imaging Applications." *IEEE Antennas and Wireless Propagation Letters* (under review).
2. Molaei, A., Tirado, L., Bisulco, A., Gehrke, C., Zhu, A., & Martinez-Lorenzo, J.A. "3D Printed Conical Horn Antenna Equipped with Orbital Angular Momentum Lenses for High-Capacity Millimeter-wave Applications." *IEEE Antennas and Wireless Propagation Letters* (under review).
3. Obermeier, R. & Martinez-Lorenzo, J.A. "Sensing Matrix Design via Capacity Maximization for Block Compressive Sensing Applications." *IEEE Transactions on Computational Imaging* (under review).
4. Heredia-Juesas, J., Molaei, A., Tirado, L., & Martinez-Lorenzo, J.A. "Sectioning-based ADMM Imaging for Fast Node Communication with a Compressive Antenna." *IEEE Antennas and Wireless Propagation Letters* (under review).

C. Peer Reviewed Conference Proceedings

1. A. Molaei, J. Heredia-Juesas, L. Tirado, W. Zhang, A. Bisulco, A. Zhu, D. Cachay, A. Ghanbarzadeh Dagheyan, J. Martinez-Lorenzo, "3D Printed Compressive Horn Antenna for High-Sensing-Capacity Millimeter-Wave Imaging", CD Proc., EuCAP 2018 — XII European Conference on Antennas and Propagation, London, UK, April, 2018.
2. J.A. Martinez-Lorenzo and R. Obermeier, "High Capacity and Efficiency Optimization of Compressive Antennas for Imaging Applications", CD Proc., EuCAP 2018 — XII European Conference on Antennas and Propagation, London, UK, April, 2018.
3. Molaei, Ali, et al. "A bilayer ELC metamaterial for multi-resonant spectral coding at mm-Wave frequencies." AP-S 2017—Antennas and Propagation & USNC/URSI National Radio Science Meeting, 2017 IEEE International Symposium on. IEEE, San Diego CA, July 2017.
4. A. Molaei, J. Heredia Juesas, and J. Martinez-Lorenzo. "Single-pixel mm-wave imaging using 8-bits metamaterial-based compressive reflector antenna." AP-S 2017—Antennas and Propagation & USNC/URSI National Radio Science Meeting, 2017 IEEE International Symposium on. IEEE, San Diego CA, July 2017.

Pending –

1. Obermeier, R., & Martinez-Lorenzo, J.A. "A Capacity-based Sensing Matrix Design Method for Block

Compressive Imaging Applications." AP-S 2018—IEEE AP-S International Symposium – URSI, Boston, MA, July 2018 (accepted, to be presented).

2. Zhang, W., & Martinez-Lorenzo, J.A. "Single-frequency Material Characterization Using a Microwave Adaptive Reflect-array." AP-S 2018—IEEE AP-S International Symposium – URSI, Boston, MA, July 2018 (accepted, to be presented).
3. Molaei, A., & Martinez-Lorenzo, J.A. "Waveguide-fed Antipodal Vivaldi Antenna using an Antipodal Finline Transition." AP-S 2018—IEEE AP-S International Symposium – URSI, Boston, MA, July 2018 (accepted, to be presented).
4. Molaei, A., & Martinez-Lorenzo, J.A. "A Low Cost Reflect Array for Near-field Millimeter-Wave Beam Focusing Applications." AP-S 2018—IEEE AP-S International Symposium – URSI, Boston, MA, July 2018 (accepted, to be presented).
5. Molaei, A., Graham, K., Tirado, L., Ghanbarzadeh, A., Bisulco, A., Heredia-Juesas, J., Liu, C., Von Holtenz, J., & Martinez-Lorenzo, J.A. "Experimental Results of a Compressive Reflector Antenna Producing Spatial Coding." AP-S 2018—IEEE AP-S International Symposium – URSI, Boston, MA, July 2018 (accepted, to be presented).
6. Heredia-Juesas, J., Tirado, L., & Martinez-Lorenzo, J.A. "Fast Source Reconstruction via ADMM with Elastic Net Regularization." AP-S 2018—IEEE AP-S International Symposium – URSI, Boston, MA, July 2018 (accepted, to be presented).
7. Heredia-Juesas, J., Molaei, A., Tirado, L., & Martinez-Lorenzo, J.A. "Fast Node Communication ADMM-based Imaging Algorithm with a Compressive Reflector Antenna." AP-S 2018—IEEE AP-S International Symposium – URSI, Boston, MA, July 2018 (accepted, to be presented).
8. L. Tirado, W. Zhang, A. Bisulco, H. Gomez-Sousa, J.A. Martinez-Lorenzo, "Towards Three-dimensional Millimeter-Wave Radar Imaging of On-the-move Targets", AP-S 2018—IEEE AP-S International Symposium – URSI, Boston MA, July 2018. (accepted, to be presented).

D. Other Presentations

1. Seminars
   a. Martinez-Lorenzo, J.A. "High Capacity and Efficiency Optimization of Compressive Antennas for Imaging Applications." European Conference on Antennas and Propagation. London, UK, 10 March 2018. Invited talk.
   b. Martinez-Lorenzo, J.A. "Research at SICA-LAB: Sensing, Imaging, (AI)-Control, and Actuation Laboratory." NU Meeting with Leddartech, Northeastern University, Boston, MA, 19 April 2018.
   c. Martinez-Lorenzo, J.A. "Imaging at Speed." NU Meeting with Transportation Security Administration Administrator David Pekoske, Northeastern University, Boston, MA, 18 May 2018.
   d. Martinez-Lorenzo, J.A. "Research at the SICA-Lab." NU-ALERT Research Experience for Undergraduates, Northeastern University, Boston, MA, 4 June 2018.
   e. Martinez-Lorenzo, J.A. "4D-Coded Compressive Systems for High-Capacity Sensing and Imaging." ECE at Michigan State University, 04 June 2018.
   f. Martinez-Lorenzo, J.A. "Next Generation Checkpoints for On-The-Move Threat Detection." Advanced Development for Security Applications (ADSA) Workshop 18, Boston, MA, 15 May 2018.
2. Poster Sessions
   a. Molaei, A., Graham, K., Heredia-Juesas, J., Tirado, L., Zhang, W., Bisulco, A., Liu, C., Von Holten, J., Zhu, A., Cachay, D., Ghanbarzadeh Dagheyan, A., & Martinez-Lorenzo, J.A. "Compressive Antennas

for High-Sensing Capacity Imaging Applications." *RISE 2018*, Northeastern University, Boston, MA, 5 April 2018.

b. Tirado, L., Zhang, W., Molaei, A., Bisulco, A., Gomez-Sousa, H., & Martinez-Lorenzo, J.A. "Three-dimensional On-the-Move Imaging Using a Millimeter-Wave CRA." *RISE 2018*, Northeastern University, Boston, MA, 5 April 2018.

3. Interviews and/or News Articles

a. Research featured by News@Northeastern. (May, 2018). "The next update to TSA checkpoints could start at Northeastern: David Pekoske visits SICA-LAB." https://news.northeastern.edu/2018/05/18/the-next-update-to-tsa-checkpoints-could-start-at-northeastern/

V. REFERENCES

[1] J. Yinon, "Field detection and monitoring of explosives," Trends in analytical chemistry, vol. 21, no. 4, pp. 415–423, 2002.
[2] J. Yinon, Forensic and Environmental Detection of Explosives. Chichester: John Wiley and Sons, 1999.
[3] M. Leahy-Hoppa, M. Fitch, X. Zheng, L. Hayden, and R. Osiander, "Wideband terahertz spectroscopy of explosives," Chemical Physics Letters, vol. 424, no. 8, pp. 227–230, 2007.
[4] D. J. Cook, B. K. Decker, and M. G. Allen, "Quantitative thz spectroscopy of explosive materials," in Optical Terahertz Science and Technology, Orlando, Florida, 14-16 March 2005.
[5] H. Liu, Y. Chen, G. J. Bastiaans, and X. Zhang, "Detection and identification of explosive rdx by thz diffuse reflection spectroscopy," Optics Express, vol. 14, pp. 415–423, 1 2006.
[6] P. Shea, T. Gozani, and H. Bozorgmanesh, "A tnt explosives-detection system in airline baggage," Nuclear Instruments and Methods in Physics Research Section A: Accelerators, Spectrometers, Detectors and Associated Equipment, vol. 299, no. 20, pp. 444–448, December 1990.
[7] C. L. Fink, B. J. Micklich, T. J. Yule, P. Humm, L. Sagalovsky, and M. M. Martin, "Nuclear instruments and methods in physics research section b: Beam interactions with materials and atoms," Evaluation of neutron techniques for illicit substance detection, vol. 99, no. 1-4, pp. 748–752, May 1995.
[8] H. Itozaki and G. Ota, "International journal on smart sensing and intelligent system," Nuclear quadrupole resonance for explosive detection, vol. 1, no. 3, pp. 705–715, September 2008.
[9] J. B. Miller and G. A. Barral, "Explosives detection with nuclear quadrupole resonance," American Scientist, vol. 93, pp. 50–57, January-February 2005.
[10] Y. Alvarez, J. A. Martinez-Lorenzo, F. Las-Heras, and C. M. Rappaport, "An inverse fast multipole method for geometry reconstruction using scattered field information," Antennas and Propagation, IEEE Transactions on, vol. 60, no. 7, pp. 3351–3360, 2012.
[11] J. Martinez-Lorenzo, J. Heredia Juesas, and W. Blackwell, "A single transceiver compressive reflector antenna for high-sensing-capacity imaging," Antennas and Wireless Propagation Letters, IEEE, vol. PP, no. 99,pp. 1–1, 2015.
[12] J. Heredia Juesas, G. Allan, A. Molaei, L. Tirado, W. Blackwell, and J. Martinez Lorenzo, "Consensus based imaging using admm for a compressive reflector antenna," in Antennas and Propagation & USNC/URSI National Radio Science Meeting, 2015 IEEE International Symposium on. IEEE, 2015, pp. 1304–1305.
[13] J. Heredia-Juesas, A. Molaei, L. Tirado, W. Blackwell, J.A. Martinez-Lorenzo, "Norm-1 Regularized Consensus-based ADMM for Imaging with a Compressive Antenna." *IEEE Antennas and Wireless Propagation Letters*, *PP*(99), June 2017.
[14] J. Heredia-Juesas, L. Tirado, J.A. Martinez-Lorenzo, "Fast Source Reconstruction via ADMM with Elastic Net Regularization", AP-S 2018—IEEE AP-S International Symposium – URSI, Boston MA, July 2018. (Accepted, to be presented).
[15] R. Obermeier and J. A. Martinez-Lorenzo, "Sensing Matrix Design via Mutual Coherence Minimization for Electromagnetic Compressive Imaging Applications," *IEEE Transactions on Computational Imaging*, vol.

3, no. 2, pp. 217-229, 2017.
[16] R. Obermeier and J. A. Martinez-Lorenzo, "Sensing Matrix Design via Capacity Maximization for Block Compressive Sensing Applications," *IEEE Transactions on Computational Imaging*, 2018 (In Review).
[17] R. Obermeier and J. A. Martinez-Lorenzo, "A Capacity-based Sensing Matrix Design Method for Block Compressive Imaging Applications," in IEEE International Symposium on Antennas and Propagation and USNC-URSI Radio Science Meeting, Boston, MA, 2018.
[18] M. Zhou, S. B. Sørensen, E. Jørgensen, P. Meincke, O. S. Kim, and O. Breinbjerg, "Analysis of printed reflect arrays using extended local periodicity," in Antennas and Propagation (EUCAP), Proceedings of the 5th European Conference on. IEEE, pp. 1408–1412, 2011.
[19] S. Becker, J. Bobin, and E. J. Candes, "Nesta: a fast and accurate firstorder method for sparse recovery," *SIAM Journal on Imaging Sciences*, vol. 4, no. 1, pp. 1–39, 2011.
[20] R. Obermeier and J. A. Martinez-Lorenzo, "Physicality constrained compressive sensing algorithm for electromagnetic imaging applications," in Antennas and Propagation (APSURSI), 2016 IEEE International Symposium, 2016.
[21] R. Obermeier and J. A. Martinez-Lorenzo, "Sensing Matrix Design via Mutual Coherence Minimization for Electromagnetic Compressive Imaging Applications," IEEE Transactions on Computational Imaging, vol. 3, no. 2, pp. 217-229, 2017.
[22] G. Lockwood and F. S. Foster, "Optimizing sparse two-dimensional transducer arrays using an effective aperture approach," in Ultrasonics Symposium, 1994. Proceedings., 1994 IEEE, vol. 3. IEEE, 1994, pp. 1497–1501.
[23] S. S. Ahmed, A. Schiess, and L.-P. Schmidt, "Near field mm-wave imaging with multistatic sparse 2d-arrays," in 2009 European Radar Conference (EuRAD), 2009.
[24] C. Watts, "Metamaterials and their applications towards novel imaging technologies," Ph.D. dissertation, PhD Thesis, 2015.
[25] T. Sleasman, M. Boyarsk, M. F. Imani, J. N. Gollub, and D. R. Smith, "Design considerations for a dynamic metamaterial aperture for computational imaging at microwave frequencies," JOSA B, vol. 33, no. 6, pp. 1098–1111, 2016.
[26] E. Byron, "Radar principles, technology, applications," Englewood Cliffs, New Jersey: PTR Prentice hall, pp. 618–627, 1993.
[27] S. S. Ahmed, A. Schiessl, and L.-P. Schmidt, "Multistatic mm-wave imaging with planar 2d-arrays," in 2009 German Microwave Conference. IEEE, 2009, pp. 1–4.